A model of mechanical loading of the lungs including gravity and a balancing heterogeneous pleural pressure

Alice Peyraut, Martin Genet

A model of mechanical loading of the lungs including gravity and a balancing heterogeneous pleural pressure

A. Peyraut[1,2] and M. Genet[1,2]

[1] *Solid Mechanics Laboratory, École Polytechnique/IPP/CNRS, France*
[2] *MΞDISIM Team, INRIA, France*

July 27, 2024

Contents

Abstract

Recent years have seen the development of multiple *in silico* lung models, notably with the aim of improving patient care for pulmonary diseases. These models vary in complexity, and typically only consider the implementation of pleural pressure, a depression that keeps the lungs inflated. Gravity, often considered negligible compared to pleural pressure, has been largely overlooked, also due to the complexity of formulating physiological boundary conditions to counterbalance it. However, gravity is known to affect pulmonary functions, such as ventilation. In this study, we incorporated gravity into a recent lung poromechanical model. To do so, in addition to the gravitational body force, we proposed novel boundary conditions consisting in a heterogeneous pleural pressure field constrained to counterbalance gravity to reach global equilibrium of applied forces. We assessed the impact of gravity on the global and local behavior of the model, including the pressure-volume response and porosity field. Our findings reveal that gravity, despite being small, influences lung response. Specifically, the inclusion of gravity in our model led to the emergence of heterogeneities in deformation and stress distribution, compatible with *in vivo* imaging data. This could provide valuable insights for predicting the progression of certain pulmonary diseases by correlating areas subjected to higher deformation and stresses with disease evolution patterns.

Keywords

Pulmonary mechanics; Gravity; Modeling; Constrained optimization; Finite element method.

1 Introduction

Idiopathic Pulmonary Fibrosis (IPF) is an interstitial lung disease, characterized by increased difficulty for patients to breath [Swigris et al. 2005]. Although a rare disease, its impact has grown over the last few decades, becoming an important health burden [Nalysnyk et al. 2012; Hutchinson et al. 2015], especially as no cure is known as of today [Spagnolo et al. 2018; Wells 2018]. As an idiopathic disease, the mechanisms behind the appearance and evolution of IPF still remain unclear. However, the existence of a mechanical vicious circle that could explain the evolution of IPF has been hypothesized [Liu et al. 2010; Hinz et al. 2016; Wu et al. 2020]. This disease is indeed characterized by a stiffening of localized areas of the interstitial tissue of the lungs, i.e., the appearance of fibrosed tissue [Plantier et al. 2018; Wijsenbeek et al. 2020], which induces larger —non-physiological— stresses during breathing, and could in turn injure the healthy tissue, leading

to collagen deposits during repairing processes [McKleroy et al. 2013]. These collagen deposits are abnormally high in IPF and stiffen the tissues, leading to higher stresses, and so on. Although tissue stiffening in IPF is irreversible, recent breakthroughs in treatments have significantly increased patient life expectancy, making early diagnosis a key issue in patient care [Cottin et al. 2022]. A better understanding of the disease and its progression could also help clinicians targeting the most efficient treatment and improve patient care.

In silico models are increasingly used to tackle these issues. They have indeed gained considerable interest in recent years in the medical field and have become valuable tools for doctors, as they are proved to be extremely useful to help with diagnosis and prognosis, and for improving patient care [Himanshu 2019; Carniel et al. 2020]. To handle issues related to diagnosis, prognosis or treatment, models should be patient-dependent [Vy et al. 2016; Gindre et al. 2016], as the behavior of biological tissues or organ geometries, for example, differ highly from an individual to another. Questions related to the accuracy and complexity of these models is therefore essential. In particular, for medical applications, a high level of accuracy is generally required, e.g., to predict with a good level of confidence the evolution of a disease. This is for example the case in cardiac modeling. A wide variety of models, integrating clinical data, have been developed to tackle various medical issues [Smith et al. 2011; Chabiniok, Wang, et al. 2016]. Personalized models allow to investigate, for example, various pathologies [Genet, L. C. Lee, Baillargeon, et al. 2016] or surgical procedures [L. C. Lee et al. 2014]. Similarly, a model of the lungs [Patte, Genet, et al. 2022], integrating clinical data [Genet, Patte, Fetita, et al. 2020; Patte, Brillet, et al. 2022; Laville et al. 2023], has recently been developed to improve the diagnosis, classification and prognosis of IPF.

A wide variety of lung models, each investigating various constitutive frameworks, loading and scales, can be found in the literature [Neelakantan et al. 2022]. The framework chosen to represent the deformation of the lungs depends greatly on the level of accuracy wanted. Linear elastic behaviors have been widely used to describe the deformation of the parenchyma [Fuerst et al. 2014; Werner et al. 2009], which can be an acceptable approximation within the scope of some studies. More complex frameworks, such as the one proposed by [Tawhai et al. 2009] allow to take into account the non-linear behavior of the lungs. Heterogeneity of tissue porosity in the lung has been investigated at the microscopic level [Álvarez-Barrientos et al. 2021; Manoochehrtayebi et al. 2023], who studied the microstructure of the lungs, most macroscale models of the literature but largely overlooked at the macroscopic level. We therefore chose to work within a poromechanical framework [Chapelle et al. 2014; Patte, Genet, et al. 2022], which allows us to include at all points the contributions of both the solid and the fluid, and hence the material heterogeneity resulting from the heterogeneous porosity field.

Different timescales have been investigated for the development of lung models. If dynamic models have been formulated [Kyriakou et al. 2011], we however chose to develop a quasi-static model of the lungs. Our model is indeed based on clinical data, which consists solely in two CT-scans for each patient—one at end-exhalation and one at end-inhalation. Dynamic data, for example from MRI [Boucneau et al. 2020] being unavailable for our study, our model focuses on representing a quasi-static breathing cycle, i.e., the deformation of the lungs from the end-exhalation configuration to the end-inhalation configuration.

Different techniques have also been proposed to pilot the deformation of the lungs from end-exhalation to end-inhalation, such as imposing a displacement field, obtained by image correlation, on the boundary of the lungs [Zhang et al. 2004; Berger et al. 2016] or on the parietal membrane, when a frictionless contact between the surface of the lungs and the parietal membrane is implemented [Tawhai et al. 2009]. These approaches, implemented as Dirichlet boundary conditions, do not take the pleural pressure, a negative (compared to the reference atmospheric pressure) pressure responsible for inflation of the lungs, in consideration. The pleural pressure being of particular interest in this study, since we could potentially derive biomarkers from it in future work, we chose to drive our deformation with this pleural pressure, following the example of [Baudet et al. 2003; Zhang et al. 2004; Han et al. 2017]. The distribution of the pleural pressure is discussed in this article. Its magnitude, however, will be determined to match the displacement field from end-exhalation to end-inhalation extracted from CT-scans when handling clinical cases.

Gravity has almost systematically been either neglected [Patte, Genet, et al. 2022], or only partially included [Patte 2020], in *in silico* lung models, probably for two main reasons. The first reason is that the impact of gravity is often considered to be negligible regarding other forces acting on the lungs, e.g., the pleural pressure. The second reason would be that is not always straightforward to take gravity into account, since it requires the formulation of additional boundary conditions that can balance gravity to satisfy the global equilibrium. Notably, [Seyfi Noferest et al. 2018] has proposed a model that includes gravity, but the boundary conditions —i.e., fixing the lungs at the helium— seem non-applicable for our problem. It would indeed require to identify precisely the location of those points in CT-scans, and these boundary conditions do not take into account the impact of the surroundings of the lungs on their deformation.

However, even though complex to implement, gravity does have an impact on lung response. There is indeed a pleural pressure gradient in the lungs, more negative at the apex than at the base [Barrau et al. 2022]. Lungs also behave differently in the prone and the supine position [Kallet 2015]. While it was initially assumed that gravity was responsible for differences in ventilation and blood flow between the prone and supine positions [Kaneko et al. 1966], more recent articles, such as [Galvin et al. 2007], have emphasized that the impact of gravity on these phenomena is in reality marginal. However, gravity is identified as one of the main factors causing the differences of pulmonary pressures and lung densities between the prone and supine positions [Tawhai et al. 2009; Kumaresan et al. 2018]. In addition, studies have shown that gravity induces not only local phenomena in the lungs [West and Matthews 1972; Hurtado et al. 2017], but also affects the global behavior of the lungs, e.g., its compliance [Ganesan et al. 1995]. In light of these phenomena, we therefore decided to take gravity into account in our model to improve its accuracy.

Integrating gravity into lung models therefore represents an important challenge, which we address in this article by formulating novel physiological boundary conditions including effectively gravity. For illustration purpose, the novel boundary conditions are described in the context of our poromechanical lung model [Patte, Genet, et al. 2022], though they could be applied to any lung model. Briefly, in [Patte, Genet, et al. 2022], the lung deformation was driven by the motion (prescribed arbitrarily in [Patte, Genet, et al. 2022] or extracted from clinical images in [Patte, Brillet, et al. 2022; Laville et al. 2023]) of the thoracic cage (modeled as a surface in frictionless bilateral contact with the lung volume). Previous efforts to integrate gravity in the model have been documented in [Patte 2020]; however, these attempts proved incomplete, notably because gravity was successfully implemented only for the loading problem (i.e., the computation of the end-inhalation configuration from the unloaded configuration), and not for the unloading problem (i.e., the computation of the unloaded configuration from the end-exhalation configuration). Compared to these earlier models, the boundary conditions introduced in this paper do not require contact definition nor additional geometries such as the rib cage; moreover, gravity is present at both loading and unloading computation steps. Basically, they rely on the incorporation of an additional term in the pleural pressure distribution, defined through a minimization problem enforcing the balance of gravity to satisfy the global equilibrium of the lung.

The paper is organized as follows. In the Methods Section 2, we briefly recall [Patte, Genet, et al. 2022]'s lung poromechanics framework (Section 2.1) and then introduce our new boundary conditions (Section 2.2). Next, in the Results Section 3, we propose several analysis of the model, including the impact of gravity on the computed pleural pressure distribution (Section 3.1) and the model response (Section 3.2), as well as a comparison of our new model response to experimental data (Section 3.3) and our previous model response (Section 3.4). These, results, as well as the relevance and accuracy of our proposed boundary conditions, are thoroughly discussed in the Discussion Section 4.

2 Methods

2.1 Recall of our lungs poromechanical modeling framework

As mentioned in the Introduction, the novel boundary conditions we introduce in this paper could be applied to any lung model, but are described here in the context of our lung poromechanical model, which is described in details in [Patte, Genet, et al. 2022], and is briefly recalled in this Section.

2.1.1 General hypotheses

As reminded in the Introduction, our model is quasi-static and computes the end-inhalation configuration from the end-exhalation configuration. At end-exhalation, lungs are already loaded, notably by the pleural pressure, a negative pressure keeping them inflated. (Note that in this paper, pressure is always relative to the atmospheric, i.e., a "negative" pressure corresponds to a sub-atmospheric pressure.) Computing the end-inhalation configuration from the end-exhalation configuration is therefore not straightforward. It requires two steps. The first step consists in computing the unloaded configuration from the end-exhalation configuration. In the scope of this work, we will call this problem the unloading problem. The second step consists in computing the end-inhalation configuration from the unloaded configuration. We will call this problem the loading problem. These problems are illustrated in Figure 1.

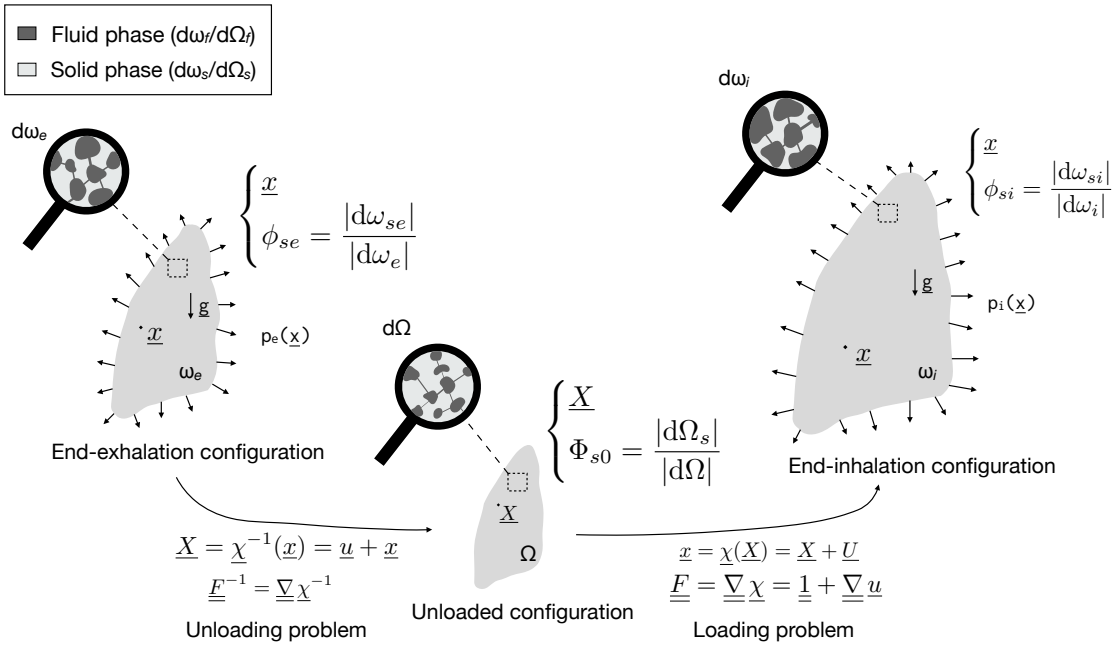

Figure 1: Description of the computation of a full breathing cycle with our finite-element model.

2.1.2 Poromechanical framework

To compute the end-inhalation configuration from the end-exhalation configuration, we chose to work within a poromechanical framework, which is consistent with experimental data and allows to integrate the porosity field extracted from the CT-scans. In this work, we consider that at each point of our domain, the matter is split into a solid phase, in our case the blood and the tissues, and a fluid phase, the air, that interact with each other. To describe the behavior of the different phases, classical kinematical and mechanical operators, as well as operators specific to poromechanics, are used. The notation used in this paper is detailed hereafter. Quantities with the subscript "e" refer to quantities defined in the end-exhalation configuration, whilst quantities with the subscript "i" refer to quantities defined in the end-inhalation configuration. Similarly, the volumes and surfaces written in capital letters represent quantities in the unloaded configuration,

whilst lowercase letters refer to quantities in loaded configurations. The operators and quantities introduced are also described in Figure 1.

Kinematics operators for the loading problem. The function $\underline{\chi}$, representing the mapping of a material point at a position $\underline{\mathrm{X}}$ in the unloaded configuration Ω to a position $\underline{\mathrm{x}}$ in the deformed configuration ω, can be written as

$$\underline{\chi} : \underline{\mathrm{X}} \rightarrow \underline{\chi}(\underline{\mathrm{X}}) = \underline{\mathrm{x}}(\underline{\mathrm{X}}). \tag{1}$$

The displacement field from the unloaded to the deformed configuration is then simply defined by the difference between the two position vectors

$$\underline{\mathrm{U}}(\underline{\mathrm{X}}) := \underline{\mathrm{x}}(\underline{\mathrm{X}}) - \underline{\mathrm{X}}. \tag{2}$$

The deformation gradient tensor can be derived from the mapping function, and is defined as

$$\underline{\underline{\mathrm{F}}} := \underline{\underline{\nabla}}\,\underline{\chi} = \underline{\underline{1}} + \underline{\underline{\nabla}}\,\underline{\mathrm{U}}. \tag{3}$$

The volume change of the mixture is in turn defined from the deformation gradient tensor:

$$\mathrm{J} := \det(\underline{\underline{\mathrm{F}}}). \tag{4}$$

In order to fully describe our problem, two additional operators need to be introduced: the right Cauchy tensor can be defined from the deformation gradient tensor:

$$\underline{\underline{\mathrm{C}}} := {}^{\mathrm{t}}\underline{\underline{\mathrm{F}}} \cdot \underline{\underline{\mathrm{F}}}, \tag{5}$$

from which the Green-Lagrange strain tensor is in turn defined:

$$\underline{\underline{\mathrm{E}}} := \frac{1}{2}(\underline{\underline{\mathrm{C}}} - \underline{\underline{1}}). \tag{6}$$

Kinematics operators for the unloading problem The operators described so far can be used for the loading problem, i.e., for computing a deformed configuration from an unloaded configuration. These operators are classical but cannot be directly used for the unloading problem, for which the unloaded configuration is unknown. Let us here describe multiple quantities that will allow us to properly define the unloading problem.

The displacement field from the deformed configuration to the unloaded configuration, written $\underline{\mathrm{u}}$, can be expressed as

$$\underline{\mathrm{u}}(\underline{\mathrm{x}}) := \underline{\mathrm{X}}(\underline{\mathrm{x}}) - \underline{\mathrm{x}}, \tag{7}$$

where the position vector $\underline{\mathrm{X}}$ in the unloaded configuration is defined through the inverse mapping function

$$\underline{\chi}^{-1} : \underline{\mathrm{x}} \rightarrow \underline{\chi}^{-1}(\underline{\mathrm{x}}) = \underline{\mathrm{X}}(\underline{\mathrm{x}}). \tag{8}$$

The deformation gradient tensor from the deformed configuration to the unloaded configuration can also be derived, in the same way as before, from the mapping function:

$$\underline{\underline{\mathrm{f}}} := \underline{\underline{\nabla}}\,\underline{\chi}^{-1}, \tag{9}$$

from which the volume change can in turn be defined:

$$\mathrm{j} := \det(\underline{\underline{\mathrm{f}}}) = \frac{1}{\mathrm{J} \circ \underline{\chi}^{-1}}. \tag{10}$$

We also define the infinitesimal strain tensor with its usual definition

$$\underline{\underline{\epsilon}} := \frac{1}{2}(\underline{\underline{\nabla}}\,\underline{\mathrm{u}} + {}^{\mathrm{t}}\underline{\underline{\nabla}}\,\underline{\mathrm{u}}). \tag{11}$$

Poromechanics operators. As a reminder, at each point of our domain, a fluid and a solid phase interact. Their proportions are defined through the volume fraction of fluid, Φ_{f}, and the volume fraction of solid, Φ_{s}. In this article, operators with the subscript "f" refer to quantities related to the fluid phase and operators with the subscript "s" refer to quantities related to the solid phase. Φ_{f} and Φ_{s} are defined as

$$\begin{cases} \Phi_{\mathrm{f}} := \dfrac{|\mathrm{d}\omega_{\mathrm{f}}|}{|\mathrm{d}\Omega|} \\ \Phi_{\mathrm{s}} := \dfrac{|\mathrm{d}\omega_{\mathrm{s}}|}{|\mathrm{d}\Omega|} \end{cases}, \tag{12}$$

where $\mathrm{d}\Omega$ corresponds to an infinitesimal volume of matter of the reference volume Ω and $\mathrm{d}\omega_{\mathrm{f}}$ and $\mathrm{d}\omega_{\mathrm{s}}$ represent an infinitesimal volume of the fluid and solid phase respectively in the deformed configuration (see Figure 1). It is here possible to notice that the Jacobian, defined in Equation (4) can be written as the sum of Φ_{s} and Φ_{f}:

$$\mathrm{J} = \frac{|\mathrm{d}\omega|}{|\mathrm{d}\Omega|} = \frac{|\mathrm{d}\omega_{\mathrm{f}}|}{|\mathrm{d}\Omega|} + \frac{|\mathrm{d}\omega_{\mathrm{s}}|}{|\mathrm{d}\Omega|} = \Phi_{\mathrm{f}} + \Phi_{\mathrm{s}}. \tag{13}$$

Other constituent volume fractions can be defined, such as

$$\begin{cases} \Phi_{\mathrm{f0}} := \dfrac{|\mathrm{d}\Omega_{\mathrm{f0}}|}{|\mathrm{d}\Omega|} \\ \Phi_{\mathrm{s0}} := \dfrac{|\mathrm{d}\Omega_{\mathrm{s0}}|}{|\mathrm{d}\Omega|} \end{cases}, \qquad \begin{cases} \phi_{\mathrm{f}} := \dfrac{|\mathrm{d}\omega_{\mathrm{f}}|}{|\mathrm{d}\omega|} \\ \phi_{\mathrm{s}} := \dfrac{|\mathrm{d}\omega_{\mathrm{s}}|}{|\mathrm{d}\omega|} \end{cases} \quad \text{and} \quad \begin{cases} \phi_{\mathrm{f0}} := \dfrac{|\mathrm{d}\Omega_{\mathrm{f0}}|}{|\mathrm{d}\omega|} \\ \phi_{\mathrm{s0}} := \dfrac{|\mathrm{d}\Omega_{\mathrm{s0}}|}{|\mathrm{d}\omega|} \end{cases}, \tag{14}$$

where $\mathrm{d}\omega$ corresponds to an infinitesimal volume of matter of the deformed volume ω. Φ_{s0} and Φ_{f0} represent the reference volume fraction, while ϕ_{s} and ϕ_{f} represent the deformed volume fraction, and ϕ_{s0} and ϕ_{f0} represent the reference volume fraction of solid and fluid respectively, pushed forward onto the deformed configuration. In this article, we will refer to ϕ_{f} as the deformed (or loaded) porosity and Φ_{f0} as the reference (or unloaded) porosity. ϕ_{s} and Φ_{s0} will be referred to as the deformed (or loaded) and reference (or unloaded) solid volume fractions, respectively.

2.1.3 Equilibrium equations

Unloading problem. In the deformed configuration, the internal and external forces must be at equilibrium. This can be expressed in weak form as the balance of the virtual work of internal and external forces:

$$\mathrm{W}_{\mathrm{int}}(\underline{\mathrm{u}}; \underline{\mathrm{u}}^*) = \mathrm{W}_{\mathrm{ext}}(\underline{\mathrm{u}}; \underline{\mathrm{u}}^*) \quad \forall\, \underline{\mathrm{u}}^*, \tag{15}$$

where $\mathrm{W}_{\mathrm{int}}$ is the so-called virtual work of internal forces:

$$\mathrm{W}_{\mathrm{int}}(\underline{\mathrm{u}}; \underline{\mathrm{u}}^*) := \int_{\omega} \underline{\underline{\sigma}}(\underline{\mathrm{u}}) : \underline{\underline{\epsilon}}(\underline{\mathrm{u}}^*)\, \mathrm{d}\omega. \tag{16}$$

Here, $\underline{\mathrm{u}}$ is the displacement field from the deformed configuration ω to the reference configuration Ω (see Figure 1), $\underline{\underline{\sigma}}$ corresponds to the Cauchy stress associated to $\underline{\mathrm{u}}$ and $\mathrm{p_f}$ (see next Section on constitutive framework), $\underline{\mathrm{u}}^*$ is to so-called virtual displacements, $\underline{\underline{\epsilon}}(\underline{\mathrm{u}}^*)$ corresponds to infinitesimal strain tensor associated to $\underline{\mathrm{u}}^*$, and $\mathrm{W}_{\mathrm{ext}}$ is the so-called virtual work of external forces. The Cauchy stress $\underline{\underline{\sigma}}$ is linked to the second Piola-Kirchhoff stress tensor $\underline{\underline{\Sigma}}$ through the relation

$$\underline{\underline{\sigma}}(\underline{\mathrm{u}}) = \mathrm{j}(\underline{\mathrm{u}})\ \underline{\underline{\mathrm{f}}}^{-1}(\underline{\mathrm{u}})\ (\underline{\underline{\Sigma}}(\underline{\mathrm{u}}) \circ \underline{\chi}^{-1})\ \ {}^{\mathrm{t}}\underline{\underline{\mathrm{f}}}^{-1}(\underline{\mathrm{u}}). \tag{17}$$

As a reminder, j corresponds here to the Jacobian describing the volume change from the deformed configuration to the unloaded configuration, and not the traditional Jacobian, which characterizes the volume change from the unloaded configuration to the deformed configuration.

Loading problem. Equation (15) is sufficient to describe the unloading problem, since the deformed configuration is known. However, the loading problem corresponds to a classical hyperelastic problem, where only the reference configuration is known, and the deformed configuration has to be determined. Following the standard Lagrangian approach, the equilibrium equation is pulled back onto the reference configuration:

$$\mathrm{W}_{\mathrm{int}}(\underline{\mathrm{U}};\underline{\mathrm{U}}^*) = \mathrm{W}_{\mathrm{ext}}(\underline{\mathrm{U}};\underline{\mathrm{U}}^*) \quad \forall\, \underline{\mathrm{U}}^*, \tag{18}$$

where

$$\mathrm{W}_{\mathrm{int}}(\underline{\mathrm{U}};\underline{\mathrm{U}}^*) := \int_\Omega \underline{\underline{\Sigma}}(\underline{\mathrm{U}}) : \mathrm{d}_{\underline{\mathrm{U}}}\,\underline{\underline{\mathrm{E}}}\cdot\underline{\mathrm{U}}^*\,\mathrm{d}\Omega. \tag{19}$$

Here, $\underline{\mathrm{U}}$ is the displacement field from the reference configuration Ω to the deformed configuration ω (see Figure 1), $\underline{\underline{\Sigma}}$ is the second Piola-Kirchhoff stress tensor, and $\mathrm{d}_{\underline{\mathrm{U}}}\,\underline{\underline{\mathrm{E}}}\cdot\underline{\mathrm{U}}^*$ is the first differential of the Green-Lagrange strain tensor.

2.1.4 Constitutive laws

Constitutive framework. According to the second principle of thermodynamics, the second Piola-Kirchhoff stress tensor is equal to the derivative of the Helmholtz free energy of the system Ψ with respect to the Green-Lagrange strain tensor $\underline{\underline{\mathrm{E}}}$. Classically, the free energy Ψ is additively split into solid Ψ_{s} and fluid Ψ_{f} contributions [Coussy 2004; Chapelle et al. 2014]. We thus have

$$\underline{\underline{\Sigma}} = \frac{\partial\Psi}{\partial\underline{\underline{\mathrm{E}}}} = \underline{\underline{\Sigma}}_{\mathrm{s}} - \mathrm{p_f}\mathrm{J}\underline{\underline{\mathrm{C}}}^{-1} \qquad \text{with} \qquad \underline{\underline{\Sigma}}_{\mathrm{s}} := \frac{\partial\Psi_{\mathrm{s}}}{\partial\underline{\underline{\mathrm{E}}}}, \tag{20}$$

where $\underline{\underline{\Sigma}}_{\mathrm{s}}$ is the so-called solid stress, and $\mathrm{p_f}$ is the internal fluid pressure field. Internal mixture equilibrium, i.e., between the solid and fluid, leads to the following additional equilibrium equation:

$$\mathrm{p_f} = -\frac{\partial\Psi_{\mathrm{s}}}{\partial\Phi_{\mathrm{s}}}. \tag{21}$$

Energy potentials. Following [Coussy 2004; Chapelle et al. 2014], we write the solid free energy as the sum of two potentials, Ψ_{skel} and Ψ_{bulk}, respectively associated to the deformation and to the pressure, to which a third potential, Ψ_{por}, notably ensuring positive porosity values, is added [Patte 2020]:

$$\Psi_{\mathrm{s}} = \Psi_{\mathrm{skel}} + \Psi_{\mathrm{bulk}} + \Psi_{\mathrm{por}}. \tag{22}$$

The choice for the expression of Ψ_{skel} and Ψ_{bulk} is based on [Patte, Genet, et al. 2022]. Thus, the potential associated to the solid deformation, Ψ_{skel}, is expressed with an exponential term, a usual choice for soft tissues [Demiray 1972; Caruel et al. 2014; Genet, Chuan Lee, et al. 2015]:

$$\Psi_{\mathrm{skel}} = \alpha(\mathrm{e}^{\delta(\mathrm{J}^2-1-2\ln\mathrm{J})}-1) + \beta_1(\mathrm{I}_1-3-2\ln(\mathrm{J}))+\beta_2(\mathrm{I}_2-3-4\ln\mathrm{J}). \tag{23}$$

And the potential describing the response of the lungs to pressure, Ψ_{bulk}, is expressed as

$$\Psi_{\mathrm{bulk}} = \kappa\left(\left(\frac{\Phi_{\mathrm{s}}}{\Phi_{\mathrm{s0}}}\right)^2 - 1 - 2\ln\left(\frac{\Phi_{\mathrm{s}}}{\Phi_{\mathrm{s0}}}\right)\right). \tag{24}$$

In these expressions, I_1 is the first invariant of $\underline{\underline{\mathrm{C}}}$, and α, β_1, β_2, δ, and κ are material constants.

A third potential needs to be added to ensure positive porosities [Coussy 2004; Chapelle et al. 2014], which is especially important, in the context of lung modeling, for the unloading problem [Patte, Genet, et al. 2022]. This potential should notably tend to $+\infty$ when the porosity (loaded or unloaded) tends to 0, representing the energy barrier require to fully collapse pores, thus preventing the model to reach negative porosities. Note that there is no need to do anything special to ensure that porosities remain below 1, as in this regime the solid deformation becomes very large,

which already represents an energy barrier thanks to the skeleton energy potential. Nevertheless, following [Patte, Genet, et al. 2022], we propose to express the pore energy as:

$$\Psi_{\text{por}} = \eta \begin{cases} +\infty & \text{if} \quad \Phi_{\text{f}} < 0 \quad \text{or} \quad \Phi_{\text{f0}} < 0 \\ (\Phi_{\text{f0}}/\Phi_{\text{f}} - 1)^2 & \text{if} \quad \Phi_{\text{f}} < \Phi_{\text{f0}} \\ (\Phi_{\text{f}}/\Phi_{\text{f0}} - 1)^2 & \text{if} \quad \Phi_{\text{f0}} < \Phi_{\text{f}} \end{cases}, \tag{25}$$

where η is a material constant.

2.1.5 Weak formulation of the loading and unloading problems

Unloading problem. Combining all previous definitions and hypotheses, the unloading problem can be written as a coupled system of partial differential equations written on the deformed configuration, which is known in this case. Its weak formulation is:

$$(\underline{\mathrm{u}}, \phi_{\text{s0}}) \quad | \quad \begin{cases} \displaystyle\int_\omega \underline{\underline{\sigma}}_{\text{s}} : \underline{\underline{\epsilon}}(\underline{\mathrm{u}}^*)\,\mathrm{d}\omega - \int_\omega \mathrm{p_f}\ \mathrm{tr}(\underline{\underline{\epsilon}}(\underline{\mathrm{u}}^*))\,\mathrm{d}\omega = \mathrm{W_{ext}}(\underline{\mathrm{u}}; \underline{\mathrm{u}}^*) \quad \forall\, \underline{\mathrm{u}}^* \\ \displaystyle\int_\omega (\mathrm{p_f} + \frac{\partial \Psi_{\text{s}}}{\partial \Phi_{\text{s}}})\phi^*_{\text{s0}}\,\mathrm{d}\omega = 0 \quad \forall\, \phi^*_{\text{s0}} \end{cases} . \tag{26}$$

Let us point out that Equation (21) is local; however, it is written here in weak form for consistency in notations and to have a formulation as close as possible to our numerical implementation.

Loading problem. The loading problem is obtained by pulling back these equations onto the reference configuration, which is known in this case:

$$(\underline{\mathrm{U}}, \Phi_{\text{s}}) \quad | \quad \begin{cases} \displaystyle\int_\Omega \underline{\underline{\Sigma}}_{\text{s}} : \mathrm{d}_{\underline{\mathrm{U}}}\underline{\underline{\mathrm{E}}} \cdot \underline{\mathrm{U}}^*\,\mathrm{d}\Omega - \int_\Omega \mathrm{p_f J}\underline{\underline{\mathrm{C}}}^{-1} : \mathrm{d}_{\underline{\mathrm{U}}}\underline{\underline{\mathrm{E}}} \cdot \underline{\mathrm{U}}^*\,\mathrm{d}\Omega = \mathrm{W_{ext}}(\underline{\mathrm{U}}; \underline{\mathrm{U}}^*) \quad \forall\, \underline{\mathrm{U}}^* \\ \displaystyle\int_\Omega (\mathrm{p_f} + \frac{\partial \Psi_{\text{s}}}{\partial \Phi_{\text{s}}})\Phi^*_{\text{s}}\,\mathrm{d}\Omega = 0 \quad \forall\, \Phi^*_{\text{s}} \end{cases} . \tag{27}$$

2.2 Introducing gravity and a balancing pleural pressure

In the previous Section, we described all operators and potentials used for the virtual work of internal forces. The virtual work of external forces is now described in this Section, which focuses on the formulation of our novel boundary conditions.

2.2.1 General expression of the virtual work of external forces

We consider two main forces applied onto the lungs. The first force is the pleural pressure, a negative pressure due to a depression in the pleural cavity. The pleural pressure keeps the lungs inflated, and becomes more negative during inhalation. The second considered force is gravity, often neglected but that we chose to take into account to improve the physiological relevance of our model. The virtual work of external forces, $\mathrm{W_{ext}}$, can therefore be written as:

$$\mathrm{W_{ext}} = \int_\omega \rho\phi_{\text{s}}\underline{\mathrm{g}}\underline{\mathrm{u}}^*\,\mathrm{d}\omega + \int_\gamma -\mathrm{p_{pl}}\underline{\mathrm{n}}\,\underline{\mathrm{u}}^*\,\mathrm{d}\gamma \tag{28}$$

where $\gamma := \partial\omega$ is the external surface of the domain in the deformed configuration ω, $\underline{\mathrm{n}}$ is the surface normal in the deformed configuration, $\mathrm{p_{pl}}$ is the pleural pressure field, $\underline{\mathrm{g}}$ is the acceleration of gravity, and ρ is the density of the solid phase. The density considered is only the density of the solid phase since the density of the fluid phase, i.e., the density of the air, is much smaller than the density of the solid phase, i.e., the density of the blood and the tissues. The impact of the weight of the fluid is hence neglected.

2.2.2 Definition of the balancing pleural pressure field

Integrating gravity in our model requires the formulation of a counterbalancing loading to ensure global equilibrium of applied forces. Considering the explicit modeling of the fixations of the lungs to its surroundings could be considered in a first approach. This approach would, however, be far too complex to implement. Because of the physiological complexity of the surroundings of organs, their fixations are indeed often dismissed in biomechanics [Chabiniok, Moireau, et al. 2012; Genet, L. C. Lee, Nguyen, et al. 2014]. Solutions, such as using linear springs [Moireau et al. 2012; Pfaller et al. 2020], have been proposed in the literature. Choosing a proper value for the stiffness of the springs is, however, always difficult.

Physiologically, gravity is balanced in the lungs by the pleural pressure gradient and by the reaction forces of the surroundings of the lungs. It therefore seemed reasonable to hypothesize that these reaction forces —some distributed, some localized, e.g., reaction at the hilum, friction against the visceral pleura, etc.— could be approximated as a heterogeneous pressure field on the external surface of the lungs. We therefore chose to formulate a pressure that could balance gravity as a boundary condition. To have a boundary condition as physiological as possible, we chose to constrain this boundary pressure to be as regular as possible, i.e., to have a surface gradient as close as possible to the physiological pressure gradient already existing in the lungs.

In order to balance gravity, the boundary pressure field should also verify the forces and momentum equilibrium. In addition, the magnitude of the boundary pressure field, i.e., its surface average value, should match the one of the reference pleural pressure field. The problem can therefore be written as a minimization problem:

$$\mathrm{p_{pl}} = \underset{\left\{ \mathrm{p \text{ such that}} \begin{cases} \int_\omega \rho\phi_\mathrm{s}\underline{\mathrm{g}}\,\mathrm{d}\omega - \int_\gamma \mathrm{p}\underline{\mathrm{n}}\,\mathrm{d}\gamma = \underline{0} \\ \int_\gamma \underline{\tilde{\mathrm{x}}} \times \mathrm{p}\underline{\mathrm{n}}\,\mathrm{d}\gamma = \underline{0} \\ \int_\gamma (\mathrm{p} - \tilde{\mathrm{p}}_\mathrm{pl})\,\mathrm{d}\gamma = \underline{0} \end{cases} \right\}}{\operatorname{argmin}} \left\{ \frac{1}{2} \int_\gamma \left(\underline{\nabla}_\mathrm{s}\mathrm{p} - \underline{\nabla}_\mathrm{s}\tilde{\mathrm{p}}_\mathrm{pl} \right)^2 \mathrm{d}\gamma \right\} \tag{29}$$

where $\tilde{\mathrm{p}}_\mathrm{pl}$ represents a reference pleural pressure field and $\underline{\tilde{\mathrm{x}}} := \begin{pmatrix} \tilde{\mathrm{x}} \\ \tilde{\mathrm{y}} \\ \tilde{\mathrm{z}} \end{pmatrix}$ corresponds to the center of mass of the structure.

2.2.3 Expression of the reference pleural pressure field

Simple model. In previous approaches, we implemented the pleural pressure as a constant [Patte, Genet, et al. 2022]. However, the pleural pressure of the lungs is known to be heterogeneous, notably because of gravity [Barrau et al. 2022]. Moreover, [Glaister et al. 1975] observed that the lung compliance decreased as the acceleration of gravity applied increased. There therefore seems to be a direct relationship between gravity and the response of the lungs. In a first approach, we propose a simple model with only a linear gradient in the direction of application of gravity, which we denote by z:

$$\tilde{\mathrm{p}}_\mathrm{pl} = \tilde{\mathrm{p}}_0 + \mathrm{K}(\mathrm{z} - \tilde{\mathrm{z}}), \tag{30}$$

where $\tilde{\mathrm{p}}_0$ and K are constants. The linear vertical gradient corresponding to the hydrostatic pressure distribution within the pleural fluid, we chose $\mathrm{K} = \rho_\mathrm{pl}\mathrm{g}$, with ρ_pl the density of the pleural liquid and g the acceleration of gravity. Thus, this model has basically one degree of freedom, $\tilde{\mathrm{p}}_0$, which controls the magnitude of the reference pleural pressure.

Introducing perturbations for ventral and thoracic respirations. However, people can breathe in very different manners, for instance using diaphragmatic vs. costal respirations, which cannot be described with the above simple model. In principle one could use a complex reference pleural pressure field, obtained by modeling the lung surrounding, or from images, but here only aim at characterizing the impact of reference pleural pressure field spatial variations onto the lung response. Hence, we propose to modify the expression of the pleural pressure presented previously by adding a term along the thoracic axis, which we denote by y:

$$\tilde{\mathrm{p}}_\mathrm{pl} = \tilde{\mathrm{p}}_0 + \mathrm{K}(\mathrm{z} - \tilde{\mathrm{z}}) - \mathrm{H}(\mathrm{y} - \tilde{\mathrm{y}})^2, \tag{31}$$

where H is a parameter. If H is positive, Equation (31) represents "diaphragmatic" breathing, while it represents "costal" breathing if H is negative. Note that y and z can be aligned in some cases, e.g., in the upright position.

These expressions are only preliminary propositions to take the different types of breathing into account. We are well aware that the formulations we propose here are insufficient to describe the real physiological behavior of the lungs; again, they were only proposed to study the impact of different types of breathing on the response of the lungs, and further investigations of better forms of pleural pressure accounting for costal and diaphragmatic breathing will be investigated in future work. Given the obvious limitations of the formulations we propose in this work, we will refer to the expression accounting —preliminarily— for the costal breathing as ventral breathing and for the diaphragmatic breathing as thoracic breathing. In the rest of the study, if there is no mention of the type of breathing, $\tilde{\mathrm{p}}_{\mathrm{pl}}$ is considered to be of the form of the simple breathing, i.e., with $\mathrm{H} = 0$.

2.2.4 Weak formulation of the full loading and unloading problems

Unloading problem. To solve the constrained minimization problem (29), the Lagrange multipliers method was used. To write the Lagrangian function associated to our problem, three additional global variables $\underline{\lambda}$, $\underline{\mu}$ and δ are introduced, which are additional unknowns. The Lagrangian function can be written as:

$$\mathcal{L}(\mathrm{p}, \underline{\lambda}, \underline{\mu}, \delta) = \frac{1}{2}\int_\gamma (\underline{\nabla}_{\mathrm{s}}\mathrm{p} - \underline{\nabla}_{\mathrm{s}}\tilde{\mathrm{p}}_{\mathrm{pl}})^2 \mathrm{d}\gamma + \underline{\lambda}\cdot\Big(\int_\omega \rho\phi_{\mathrm{s}}\underline{\mathrm{g}}\,\mathrm{d}\omega - \int_\gamma \mathrm{p}\underline{\mathrm{n}}\,\mathrm{d}\gamma\Big) + \underline{\mu}\cdot\int_\gamma (\underline{\mathrm{x}} - \tilde{\underline{\mathrm{x}}})\times \mathrm{p}\underline{\mathrm{n}}\,\mathrm{d}\gamma + \delta\int_\gamma (\mathrm{p} - \tilde{\mathrm{p}}_{\mathrm{pl}})\,\mathrm{d}\gamma. \tag{32}$$

The stationary points can be found by deriving Equation (32) with respect to p, $\underline{\lambda}$, $\underline{\mu}$ and δ, which allows to rewrite Equation (29) as a system of partial differential equations:

$$(\mathrm{p}, \underline{\lambda}, \underline{\mu}, \delta) \quad | \quad \begin{cases} \displaystyle\int_\gamma (\underline{\nabla}_{\mathrm{s}}\mathrm{p} - \underline{\nabla}_{\mathrm{s}}\tilde{\mathrm{p}}_{\mathrm{pl}})\cdot\underline{\nabla}_{\mathrm{s}}\mathrm{p}^*\mathrm{d}\gamma - \underline{\lambda}\cdot\int_\gamma \mathrm{p}^*\underline{\mathrm{n}}\,\mathrm{d}\gamma \\ \qquad\qquad + \underline{\mu}\cdot\displaystyle\int_\gamma (\underline{\mathrm{x}} - \tilde{\underline{\mathrm{x}}})\times\mathrm{p}^*\underline{\mathrm{n}}\,\mathrm{d}\gamma + \delta\int_\gamma \mathrm{p}^*\mathrm{d}\gamma = 0 \quad \forall\,\mathrm{p}^* \\ \displaystyle\int_\omega \rho\phi_{\mathrm{s}}\underline{\mathrm{g}}\,\mathrm{d}\omega - \int_\gamma \mathrm{p}\underline{\mathrm{n}}\,\mathrm{d}\gamma = 0 \\ \displaystyle\int_\gamma (\underline{\mathrm{x}} - \tilde{\underline{\mathrm{x}}})\times\mathrm{p}\underline{\mathrm{n}}\,\mathrm{d}\gamma = 0 \\ \displaystyle\int_\gamma (\mathrm{p} - \tilde{\mathrm{p}}_{\mathrm{pl}})\,\mathrm{d}\gamma = 0 \end{cases} . \tag{33}$$

Equation (33) can then be injected into Equation (26). The full unloading problem can therefore be expressed with the following weak formulation:

$$(\underline{u}, \phi_{s0}, p, \underline{\lambda}, \underline{\mu}, \delta) \quad | \quad \begin{cases} \displaystyle\int_\omega \underline{\underline{\sigma}}_s : \underline{\underline{\epsilon}}(\underline{u}^*)\, d\omega - \int_\omega p_f \,\mathrm{tr}(\underline{\underline{\epsilon}}(\underline{u}^*))\, d\omega \\ \qquad\qquad = \displaystyle\int_\omega \rho\phi_s \underline{g} \cdot \underline{u}^*\, d\omega - \int_\gamma p\underline{n} \cdot \underline{u}^*\, d\gamma \quad \forall \underline{u}^* \\ \displaystyle\int_\omega (p_f + \frac{\partial \Psi}{\partial \Phi_s}) \phi_{s0}^*\, d\omega = 0 \quad \forall\, \phi_{s0}^* \\ \displaystyle\int_\gamma (\underline{\nabla}_s p - \underline{\nabla}_s \tilde{p}_{pl}) \cdot \underline{\nabla}_s p^* d\gamma - \underline{\lambda} \cdot \int_\gamma p^* \underline{n}\, d\gamma \\ \qquad + \underline{\mu} \cdot \displaystyle\int_\gamma (\underline{x} - \underline{\tilde{x}}) \times p^* \underline{n}\, d\gamma + \delta \int_\gamma p^* d\gamma = 0 \quad \forall\, p^* \\ \displaystyle\int_\omega \rho\phi_s \underline{g} \cdot \underline{\lambda}^*\, d\omega - \int_\gamma p\underline{n} \cdot \underline{\lambda}^*\, d\gamma = 0 \quad \forall\, \underline{\lambda}^* \\ \displaystyle\int_\gamma (\underline{x} - \underline{\tilde{x}}) \times p\underline{n} \cdot \underline{\mu}^*\, d\gamma = 0 \quad \forall\, \underline{\mu}^* \\ \displaystyle\int_\gamma (p - \tilde{p}_{pl})\, \delta^*\, d\gamma = 0 \quad \forall\, \delta^* \end{cases} . \tag{34}$$

As discussed in Section 2.1.5, all equations are written in weak form, for consistency and closeness to the numerical implementation. Note that in this system, only the first two equations were already present in the model of [Patte, Genet, et al. 2022]; our novel boundary conditions lead to the formulation of the four following equations.

Loading problem. Problem (34) can be used as is for the unloading problem. However, the deformed configuration being unknown in the loading problem, it needs to be pulled back onto the reference configuration. These transformations are classical and lead to the following system:

$$(\underline{U}, \Phi_f, p, \underline{\lambda}, \underline{\mu}, \delta, \underline{\tilde{x}}) \quad | \quad \begin{cases} \displaystyle\int_\Omega \underline{\underline{\Sigma}}_s : d_{\underline{U}} \underline{\underline{E}} \cdot \underline{U}^*\, d\Omega - \int_\Omega p_f J \underline{\underline{C}}^{-1} : d_{\underline{U}} \underline{\underline{E}} \cdot \underline{U}^*\, d\Omega \\ \qquad\qquad = \displaystyle\int_\Omega \rho\Phi_{s0} \underline{g} \cdot \underline{U}^*\, d\Omega - \int_\Gamma p\, J\underline{\underline{F}}^{-T} \cdot \underline{N} \cdot \underline{U}^* d\Gamma \quad \forall\, \underline{U}^* \\ \displaystyle\int_\Omega (p_f + \frac{\partial \Psi}{\partial \Phi_s}) \Phi_f^*\, d\Omega = 0 \quad \forall\, \Phi_f^* \\ \displaystyle\int_\Gamma \underline{\underline{F}}^{-T} \cdot (\underline{\nabla}_s p - \underline{\nabla}_s \tilde{p}_{pl}) \cdot \underline{\underline{F}}^{-T} \cdot \underline{\nabla}_s p^*\, J \|\underline{\underline{F}}^{-T} \underline{N}\|\, d\Gamma - \underline{\lambda} \cdot \int_\Gamma J\underline{\underline{F}}^{-T} \underline{N}\, p^*\, d\Gamma \\ \qquad - \underline{\mu} \cdot \displaystyle\int_\Gamma (\underline{X} + \underline{U} - \underline{\tilde{x}}) \times J\underline{\underline{F}}^{-T} \underline{N}\, p^*\, d\Gamma + \delta \int_\Gamma J \|\underline{\underline{F}}^{-T} \underline{N}\| p^*\, d\Gamma = 0 \quad \forall\, p^* \\ \displaystyle\int_\Omega \rho\Phi_{s0} \underline{g} \cdot \underline{\lambda}^*\, d\Omega - \int_\Gamma pJ\underline{\underline{F}}^{-T} \underline{N} \cdot \underline{\lambda}^*\, d\Gamma = 0 \quad \forall\, \underline{\lambda}^* \\ \displaystyle\int_\Gamma (\underline{X} + \underline{U} - \underline{\tilde{x}}) \times pJ\underline{\underline{F}}^{-T} \underline{N} \cdot \underline{\mu}^*\, d\Gamma = 0 \quad \forall\, \underline{\mu}^* \\ \displaystyle\int_\Gamma (p - \tilde{p}_{pl}) J \|\underline{\underline{F}}^{-T} \underline{N}\| \delta^*\, d\Gamma = 0 \quad \forall\, \delta^* \\ \displaystyle\int_\Omega (\frac{\Phi_{s0}}{\bar{\Phi}_{s0}} (\underline{X} + \underline{U}) - \frac{\underline{\tilde{x}}}{V_0}) \underline{\tilde{x}}^*\, d\Omega = 0 \quad \forall\, \underline{\tilde{x}}^* \end{cases} \tag{35}$$

where $\Gamma := \partial\Omega$ represents the external surface of the lungs in the reference configuration, $\underline{N}$ represents the external normal in the reference configuration, $V_0 := |\Omega|$ represents the volume in the reference configuration and $\bar{\Phi}_{s0} := \frac{1}{|\Omega|} \int_\Omega \Phi_{s0} d\Omega$ represents the mean value of the solid volume fraction field in the reference configuration. Note that in this system, only the first two equations were already present in the model of [Patte, Genet, et al. 2022]; our novel boundary conditions lead to the formulation of the five following equations.

Let us point out that improving the physiological relevancy of our model by taking gravity into account induces greater computation times –computation times approximately multiplied by 6– compared to the case without gravity, i.e., the case where the loading consists in solely a homogeneous pleural pressure. However, the formulation of our new boundary conditions decrease greatly the computation times –computation times approximately divided by 6– compared to the former boundary conditions of the model, i.e., the case where boundary conditions consisted of a frictionless contact between the lungs and the rib cage. Our new boundary conditions indeed transform our original problem of two field variables (displacement and porosity) to a problem dependent on three field variables (the pleural pressure field that is defined on the lung surface) and three (for the unloading problem) or four (for the loading problem) global variables. This additional equations are, however, relatively straightforward to implement in modern finite element libraries.

Problems (34) and (35) have been implemented in an open-source finite element code [Genet, Patte, Manoochehrtayebi, et al. 2024] based on the FEniCS library [Logg et al. 2012; Alnæs et al. 2015], and is currently freely available online at `https://github.com/mgenet/dolfin_mech`.

2.3 Problem setting for model response analysis

Geometry, mesh and porosity. In the scope of this study, we investigated the influence of gravity on our model response. To do so, we used a generic model of the right lung at end-exhalation[1], corresponding to a generic patient lying in the supine position. The lung was meshed using 32416 tetrahedral elements. The geometry and mesh remain consistent with the model presented in [Patte, Genet, et al. 2022].

Loading process and porosity. It is important to note that no generic porosity field is available alongside this mesh. Thus, the actual end-exhalation and end-inhalation configurations were computed from this generic end-exhalation mesh using the following process. First, an arbitrary uniformly distributed porosity bounded by 0.6 and 0.8 was assumed in the generic end-exhalation mesh. The range [0.6, 0.8] was chosen based on (i) typical porosity values at end-inhalation –ranging from 0.7 to 0.9 in [DeGroot et al. 2018], and around 0.7 in [Yang et al. 2020]–, and (ii) the work of [Y. K. Lee et al. 2008] where densities for patients at end-exhalation appear to be approximately 1.2 times smaller than for patients at end-inhalation. The associated unloaded configuration was then computed by solving Problem (34), leading to an unphysiological porosity gradient when gravity is present in the model, despite that fact that it should correspond to a state of zero-gravity pneumothorax. To address this issue, the computed unloaded porosity was replaced by an imposed uniformly distributed porosity on the obtained unloaded mesh, bounded by 0.4 and 0.6. The range [0.4, 0.6] was chosen based on (i) the typical porosity values at end-inhalation described before, and (ii) the work of [Smit et al. 2004] where densities for patients with pneumothorax appear to be approximately 1.4 times smaller than for healthy patients. Finally, the actual end-exhalation and end-inhalation configurations were computed by solving Problem (35), leading to physiological porosity gradients when gravity is present in the model. Note that more complex and physiological porosity distributions, for instance taking into account tissue scale heterogeneities induced by the airway tree, could be straightforwardly incorporated in the model, should such data be available.

Loading constants. For both problems, the only loads considered in the scope of this model are gravity and pleural pressure. When we consider that there is no gravity, the constant g appearing in Problems (34) and (35) is set to 0, and the reference pleural pressure $\tilde{p}_{pl}$ is a constant. Conversely, when we take gravity into account, the constant g appearing in Problems (34) and (35) is chosen to be equal to its typical value, i.e., 9.81 m/s^2, and the reference pleural pressure $\tilde{p}_{pl}$ depends linearly on z (see Section 2.2.3). At end-exhalation, the mean value of the pleural pressure is around –0.5 kPa [Kallet 2015; Tawhai et al. 2009]. During normal breathing, this pressure can reach between –0.8 kPa and –1.5 kPa at end-inhalation [Mentzer et al. 2018; Patte 2020]. However, medical images are rarely acquired during normal breathing. End-inhalation images are indeed often acquired at full inspiration capacity, which corresponds to a pleural pressure that can reach –2 kPa [Patte 2020] or even –3 kPa [San Bok et al. 2018]. We therefore chose to define the mean

[1] `https://www.zygote.com`

value of our pleural pressure at –0.5 kPa at end-exhalation and –2 kPa or –3 kPa at end-inhalation, depending on the cases, cf. Tables 1 and 2.

Material constants. Our model involves many material constants, chosen to fit experimental data. Two sets of material values are used in this study. The first set of values, detailed in Table 1 is chosen to fit data from [Patte 2020], while the second set, detailed in Table 2, is chosen to fit data from [Hurtado et al. 2017].

Analyses. This article focuses on studying the impact of gravity on our model response, in the context of our novel boundary conditions. We first studied the pleural pressure distribution, with and without gravity. We then studied the impact of gravity on the global behavior of the lungs, through the investigation of the pressure-volume response, as well as its impact on the local behavior of the lungs, with the investigation of porosity distribution, with and without gravity. We focused in particular in highlighting the heterogeneities induced by gravity on the lungs, by studying the strain and stress distribution in the lungs. We notably validated our model by comparing the local deformation of the lungs with the data of [Hurtado et al. 2017]. We also conducted a comparison with our previous model to highlight the interest of the method implemented in this article. The results of all these studies are detailed in the following section.

Name	Symbol	Unit	Value
Skeleton energy parameters	α	[kPa]	[0.016, 0.16, 1.6]
	δ	[-]	0.5
	β_1	[kPa]	0.4
	β_2	[kPa]	0.2
Bulk energy parameter	κ	[kPa]	100
Pore energy parameter	η	[-]	10^{-5}
End-exhalation pleural pressure	$p_{pl,e}$	[kPa]	-0.5
End-inhalation pleural pressure	$p_{pl,i}$	[kPa]	-2.0

Table 1: Parameters used for the breathing calculations when computing the Jacobian depending on the end-inhalation pleural pressure value and when comparing our results with the results of [Patte 2020]. The parameters presented here are similar to the parameters used in [Patte, Genet, et al. 2022].

Name	Symbol	Unit	Value
Skeleton energy parameters	α	[kPa]	0.16
	δ	[-]	0.5
	β_1	[kPa]	0.8
	β_2	[kPa]	0.2
Bulk energy parameter	κ	[kPa]	100
Pore energy parameter	η	[-]	10^{-5}
End-exhalation pleural pressure	$p_{pl,e}$	[kPa]	-0.5
End-inhalation pleural pressure	$p_{pl,i}$	[kPa]	-3.0

Table 2: Parameters used for porosity calculations and for comparison with [Hurtado et al. 2017]. The parameters are based on [Patte, Genet, et al. 2022], but adapted to fit data from [Hurtado et al. 2017].

3 Results

We provide the code to reproduce the results of this paper under the form of jupyter notebooks [Peyraut et al. 2024]: static versions are given in the appendix of the paper while interactive versions are currently available online at `https://apeyraut.gitlabpages.inria.fr/gravity-modeling-paper-demos`.

3.1 Computed pleural pressure distribution

The computed pleural pressure fields are presented in Figure 2. In this figure, the value of the pressure (in kPa) on the surface of the right lung is presented at end-exhalation and at end-inhalation, for the case with and the case without gravity. The patient lying in supine position, gravity is oriented from the ventral region (denoted "V" in the figure) to the dorsal region (denoted "D" in the figure). These results show that when gravity is not taken into account, the pleural pressure is homogeneous, and equal to –0.5 kPa at end-exhalation and –3 kPa at end-inhalation, which corresponds to the values specified in our model. When gravity is taken into account, the pleural pressure takes the form of a gradient, ranging from –0.1 kPa in the dorsal region to –1 kPa in the ventral region at end-exhalation and from –2.6 kPa in the dorsal region to –3.5 kPa in the ventral region at end-inhalation. It is this gradient that balances the gravitational volume force, allowing to reach a global equilibrium.

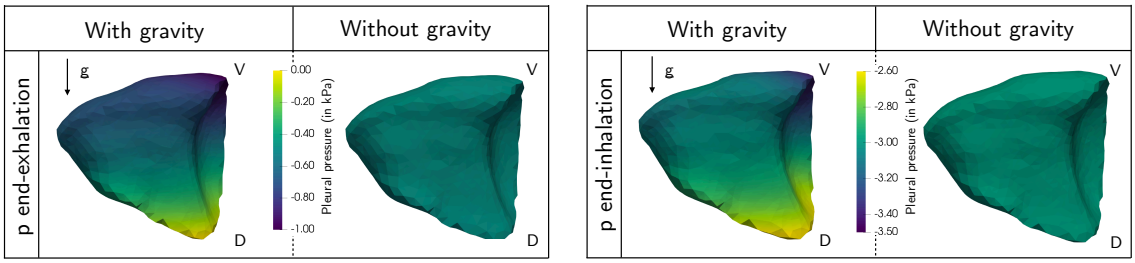

Figure 2: Pleural pressure distribution with and without gravity, at end-exhalation and end-inhalation. In our model, without gravity, the pleural pressure applied onto the lung is homogeneous. Conversely, when gravity is taken into account, a pleural pressure gradient appears, with a higher value in the ventral region than in the dorsal region.

3.2 Model response

3.2.1 Global pressure-volume response

We expect gravity to have an impact on both global and local responses of the lungs. In order to study its impact on the global response of the lungs, we chose to study the pressure-deformation response of the right lung. The change in the global pressure-deformation response of the lungs, as a function of the absolute value of the end-inhalation pleural pressure, is presented in Figure 3(a).

This figure presents the changes of volume for various values of pleural pressure at end-inhalation. The dotted lines represent the pressure-Jacobian response without gravity while the plain lines represent the pressure-Jacobian response with gravity. The Jacobian plotted in Figure 3 corresponds to the volume change from end-exhalation to end-inhalation. The study was conducted for three different values of stiffnesses, within physiological range. The curves in blue represent the response for a stiffness $\alpha = 0.016$ kPa, the curves in green represent the response for a stiffness $\alpha = 0.16$ kPa and the curves in yellow represent the response for a stiffness $\alpha = 1.6$ kPa. The values of the other parameters used in this calculation are specified in Table 1.

The pleural pressure at end-exhalation is considered to be of –0.5 kPa in the problem. For a pleural pressure at end-inhalation of –0.5 kPa, i.e., a similar loading at end-exhalation and at end-inhalation, the Jacobian is, as expected, of 1. When the end-inhalation pleural pressure is different from the end-exhalation pleural pressure, the value of the Jacobian is different with and

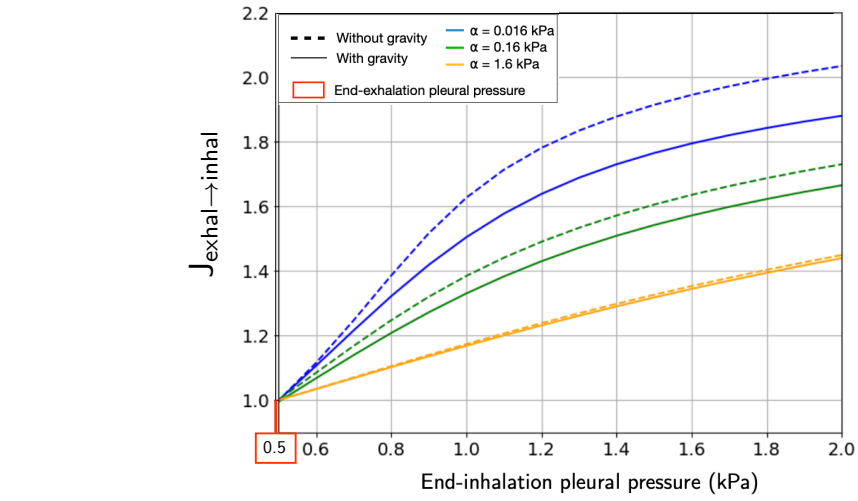

(a)

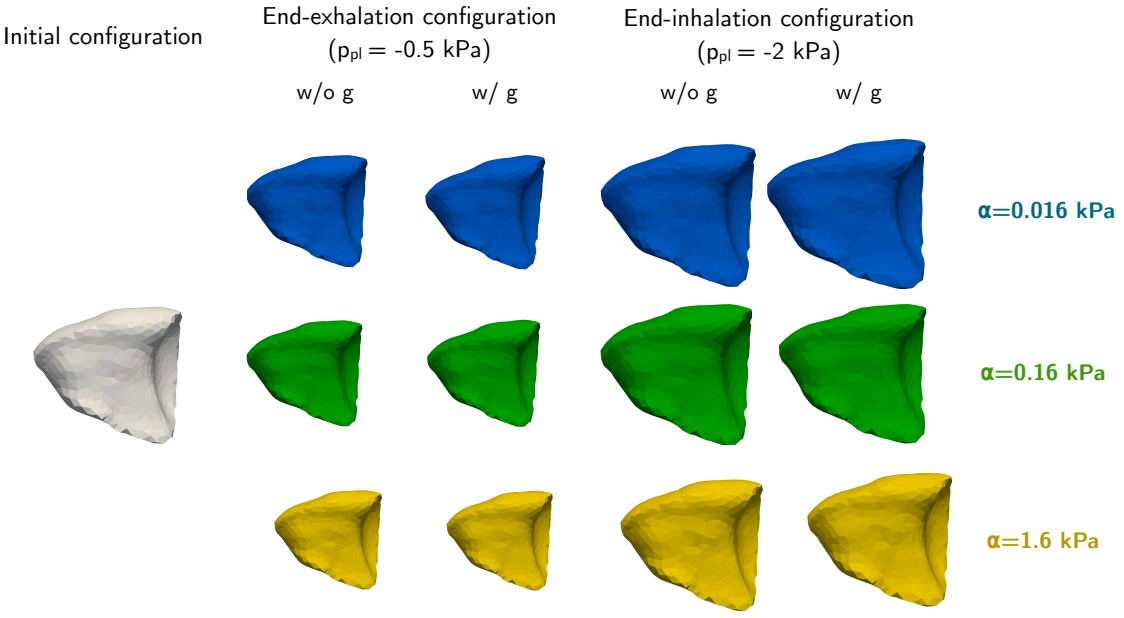

(b)

Figure 3: (a) Pressure-deformation response of the lungs for various values of stiffnesses, with and without gravity. The stiffer the tissues, the less compliant the lung. When gravity is not taken into account, the lung is more compliant. (b) Illustrations of the right lung in the cases with and without gravity for the three values of stiffnesses, and for the three configurations. The end-inhalation configuration is chosen for a pleural pressure of 2 kPa. The initial configuration (generic end-exhalation mesh) is the same for all cases.

without gravity. The maximum difference between the case with and the case without gravity for a stiffness of 1.6 kPa is indeed of 0.6%, while it is of 3% for a stiffness of 0.16 kPa and of 8% for a stiffness of 0.016 kPa. Globally, for each value of stiffness studied, the volume change from end-exhalation to end-inhalation is higher when gravity is taken into account.

Figure 3(b) illustrates the shape of the lungs for all cases. The initial generic end-exhalation configuration is the same for all cases. At "true" end-exhalation (i.e., the end-exhalation configuration computed with the porosity changes), gravity changes slightly the shape of the right lung in comparison to the case without gravity. This change is more noticeable for lower values of stiffnesses. Similarly, the shape of the right lung at end-inhalation is slightly different between the case with and the case without gravity. This change is more noticeable for lower values of stiffnesses, but barely noticeable for a stiffness of 1.6 kPa, and far less noticeable than for the end-exhalation configuration.

3.2.2 Porosity distribution

We now study the impact of gravity on various local quantities of interest of the model. First, we study the impact of gravity on the porosity, which has an influence on the macroscopic behavior of the lung tissues. The model parametrization chosen for this computation is detailed in Table 1.

Figure 4 presents the porosity maps and distributions of the right lung in the unloaded state, and the end-exhalation and end-inhalation states with and without gravity. The initial distribution, in the unloaded state is plotted in green for both graphs. Its values range from 0.4 to 0.6, resulting from the uniform law used to define the initial porosity field.

At both end-exhalation and end-inhalation, the bars in blue represent the porosity distribution without gravity and the bars in orange represent the porosity distribution with gravity. At end-exhalation, the distributions are centered around $\phi_{\mathrm{fe}} = 0.7$ when gravity is taken into account in the model and around $\phi_{\mathrm{fe}} = 0.66$ when gravity is not taken into account, which is close to the mean of the generic porosity imposed in the initial generic end-exhalation configuration. A notable difference is visible between the cases with and without gravity: in the case without gravity, the distribution remains uniform, ranging from approximately 0.58 to 0.75; on the other hand, in the case with gravity, the form of the distribution is different from the initial distribution. The distribution is much wider, with porosity values ranging from 0.42 to 0.82; it is also closer to a Gaussian than to a uniform distribution. This results from the porosity gradient visible in the end-exhalation porosity map of Figure 4, top center image.

At end-inhalation the distributions with and without gravity are very similar. The distribution seems to remain uniform in both cases, with values ranging from approximately 0.75 to 0.85. This corresponds to the near-homogeneous porosity distribution visible in the end-inhalation porosity map of Figure 4, top right image.

3.2.3 Strain distribution

To study the impact of gravity on regional deformations, we chose to plot the sagittal map of the three invariants of the right stretch tensor $\underline{\underline{U}}$. The right stretch tensor is defined through the classical polar decomposition of $\underline{\underline{F}}$ in a product of two tensors:

$$\underline{\underline{F}} = \underline{\underline{R}} \cdot \underline{\underline{U}}, \tag{36}$$

where $\underline{\underline{R}}$ is an orthogonal rotation matrix and $\underline{\underline{U}}$ is the right stretch tensor. Let us call $\mathrm{I_{1U}}$, $\mathrm{I_{2U}}$ and $\mathrm{J_U}$ the three invariants of the right stretch tensor:

$$\mathrm{I_{1U}} := \frac{1}{3}\mathrm{tr}(\underline{\underline{U}}), \quad \mathrm{I_{2U}} := \frac{1}{6}(\mathrm{tr}(\underline{\underline{U}})^2 - \mathrm{tr}(\underline{\underline{U}}^2)), \quad \mathrm{J_U} := \det(\underline{\underline{U}}). \tag{37}$$

$\mathrm{I_{1U}}$ is a measure of the length deformation, $\mathrm{I_{2U}}$ is a measure of the surface deformation and $\mathrm{J_U}$ is a measure of the volume change.

To have a complete idea of the deformation of the lungs under gravity, we also chose to study the distribution of the deviatoric strain, which is an indicator of the distortion of the tissue. The

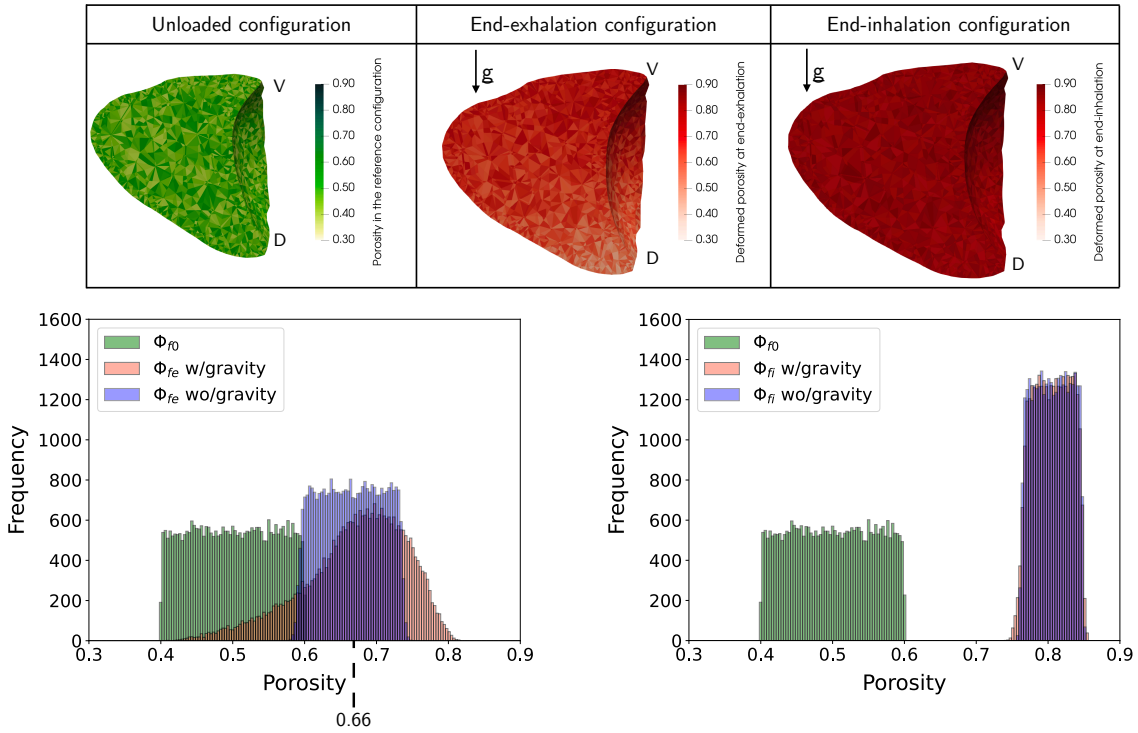

Figure 4: Top row: Prescribed porosity map in the unloaded state (left); Computed porosity maps in the end-exhalation (center) and end-inhalation (right) states, with gravity. Bottom row: Corresponding porosity distributions in unloaded state & end-exhalation (left) and unloading & end-inhalation (right), with (red) and without (blue) gravity. At end-exhalation, the distribution is wider with gravity than without gravity. At end-inhalation, the cases with and without gravity are very similar.

deviatoric strain $\underline{\underline{\mathrm{E}}}_{\mathrm{dev}}$ is classically defined as

$$\mathrm{E}_{\mathrm{dev}} := \sqrt{\frac{3}{2}\underline{\underline{\mathrm{E}}}_{\mathrm{dev}} : \underline{\underline{\mathrm{E}}}_{\mathrm{dev}}} \quad \text{with} \quad \underline{\underline{\mathrm{E}}}_{\mathrm{dev}} := \frac{1}{2}(\mathrm{J}^{-\frac{2}{3}}\underline{\underline{\mathrm{C}}} - \underline{\underline{1}}). \tag{38}$$

Figure 5 presents sagittal views of the distributions of $\mathrm{I}_{1\mathrm{U}}$, $\mathrm{I}_{2\mathrm{U}}$, J_{U} and $\mathrm{E}_{\mathrm{dev}}$. $\mathrm{I}_{1\mathrm{U}}$, $\mathrm{I}_{2\mathrm{U}}$ and J_{U} display the same behavior. The parametrization chosen for this calculation is detailed in Table 2. When there is no gravity, they are constant throughout the lungs and express an increase of each dimension—length, surface and volume–. But when there is gravity, they become heterogeneous: both length, surface and volume change increase more in the dorsal region than in the ventral region. As for the deviatoric strain, when there is no gravity, it is null as the deformation of the lung is purely volumetric. However, when there is gravity, the deviatoric strain is highly heterogeneous, with higher values localized at the base of the lung.

3.2.4 Stress distribution

To study the impact of gravity on regional stresses, we study the distributions of hydrostatic and deviatoric stresses. The hydrostatic stress is classically defined as

$$\sigma_{\mathrm{hydro}} := \sqrt{\frac{1}{3}\underline{\underline{\sigma}}_{\mathrm{hydro}} : \underline{\underline{\sigma}}_{\mathrm{hydro}}} \quad \text{with} \quad \underline{\underline{\sigma}}_{\mathrm{hydro}} := \frac{1}{3}\mathrm{tr}(\underline{\underline{\sigma}})\,\underline{\underline{1}}, \tag{39}$$

and the deviatoric stress as

$$\sigma_{\mathrm{dev}} := \sqrt{\frac{3}{2}\underline{\underline{\sigma}}_{\mathrm{dev}} : \underline{\underline{\sigma}}_{\mathrm{dev}}} \quad \text{with} \quad \underline{\underline{\sigma}}_{\mathrm{dev}} := \underline{\underline{\sigma}} - \underline{\underline{\sigma}}_{\mathrm{hydro}}. \tag{40}$$

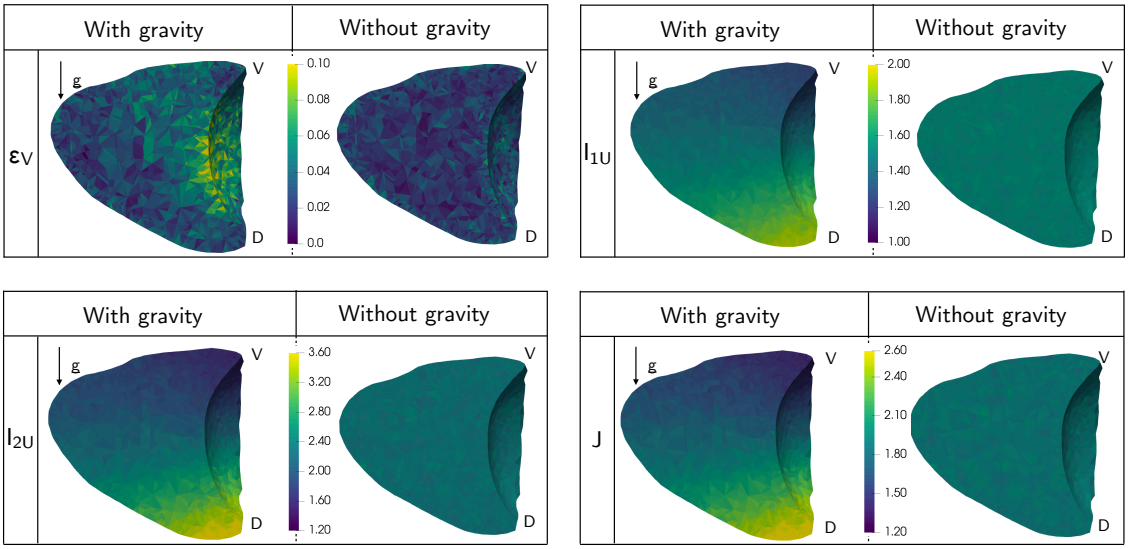

Figure 5: Sagittal maps of the deviatoric strain (top left, quantifying shear deformation), the first (top right, quantifying length change), second (bottom left, quantifying surface change) and third (bottom right, quantifying volume change) invariants of the right stretch tensor, with and without gravity. Without gravity, all quantities are homogeneous. With gravity, the length, surface and volume changes are larger in the dorsal area, while the deviatoric strain is localized at the base of the lungs.

Figure 6 presents sagittal views of the distributions of σ_{hydro} and σ_{dev}. The parametrization chosen for this calculation is detailed in Table 2. When there is no gravity in the model, the hydrostatic and deviatoric stresses are distributed relatively homogeneously in the lung. Conversely, when gravity is taken into account in the model, the hydrostatic stress take higher values in the dorsal region, while they are close to 0 in the ventral region; as for the deviatoric stress, they are localized in the dorsal region of the lung.

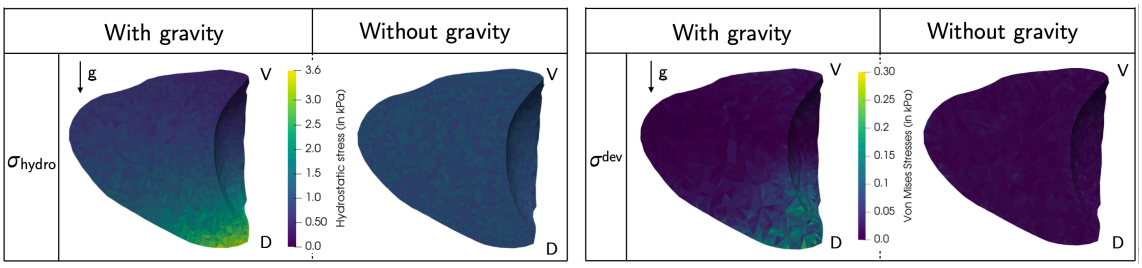

Figure 6: Sagittal maps of hydrostatic (left) and deviatoric (right) stresses, with and without gravity. When there is no gravity, the hydrostatic stresses and the deviatoric stresses are relatively homogeneous in the lung. When gravity is taken into account, higher hydrostatic and deviatoric stresses appear in the dorsal region.

3.3 Comparison with experimental data

In the previous Section, we saw that sagittal maps of porosity, strain and stress measures are highly heterogeneous when gravity is taken into account. It therefore seemed important to study such distributions, notably the strain distribution, in a more quantitative manner. Hence, we now compare the regional strain distribution predicted by our model to the one measured in [Hurtado et al. 2017], and then study the impact of some model parameters on such distribution.

Following [Hurtado et al. 2017], the strain quantities of interest —I_{1U}, I_{2U} and J_U— are first log-normalized. To do so, we first compute the maximum-likelihood estimators of the location and scale parameters of the distribution of each quantity of interest Q over the whole mesh:

$$\hat{\mu}_Q := \frac{1}{n}\sum_{k=1}^{n} \log(Q_k), \quad \text{and} \quad \hat{\sigma}_Q := \frac{1}{n}\sum_{k=1}^{n} (\log(Q_k) - \hat{\mu})^2, \tag{41}$$

where n if the number of mesh elements. Then, for each element we compute the log-normalized quantities of interest:

$$\hat{Q} := \frac{\log(Q) - \hat{\mu}_Q}{\hat{\sigma}_Q}. \tag{42}$$

Next, following the approach of [Hurtado et al. 2017; Nelson et al. 2023], we split the mesh in ten coronal zones, as shown in Figure 7—the first zone corresponds to the dorsal area ("D") while the tenth zone corresponds to the ventral area ("V"). Finally, for each zone, we compute the mean of the normalized quantities of interest.

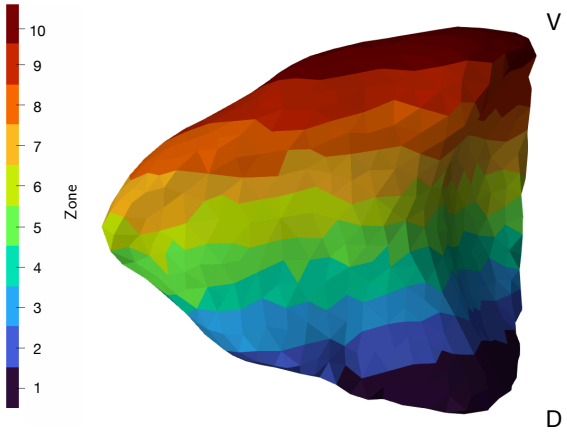

Figure 7: Definition of ten coronal zones in the right lung of a patient in supine position. The first zone corresponds to the dorsal area, denoted "D", and the tenth zone corresponds to the ventral area, denoted "V".

The log-normal distribution of the invariants in the ten coronal zones, obtained with our model (color) as well as measured by [Hurtado et al. 2017] (black boxes), is presented in Figure 8. Note that this figure only displays modeling results in the supine position (which corresponds to the experimental condition), and with gravity. Indeed, when gravity is not taken into account in the model, the three invariants are homogeneous across the coronal zones; moreover, they cannot be log-normalized as the scale parameter is equal to zero. The green curves represent the results for a purely linear reference pleural pressure ($H = 0$). The spatial evolution of the quantities of interest is consistent with the experimental data: the value of the invariants is larger in the dorsal area, and decrease as the region considered is closer to the ventral area. The values of the parameters used for this calculation can be found in Table 2. The parameters chosen were adjusted to fit better the data from [Hurtado et al. 2017].

In order to quantify the impact of the reference pleural pressure (which could be used to model ventral and thoracic breathing, as discussed in Section 2.2.3), we also considered cases with $H = H1 := \pm 0.0050$K (red and blue curves) and $H = H2 := \pm 0.0065$K (purple an yellow). The sign and magnitude of H does have an impact on the spatial evolution of the strain quantities of interest, with lower values in the dorsal region, larger ($H < 0$) or lower ($H > 0$) values in the central region, and larger ($H > 0$) or lower ($H < 0$) values in the ventral region.

3.4 Comparison with our previous model

In our former model [Patte, Genet, et al. 2022], gravity was not taken into account, even though some heterogeneity within the lung stress fields was induced by frictionless contact between the

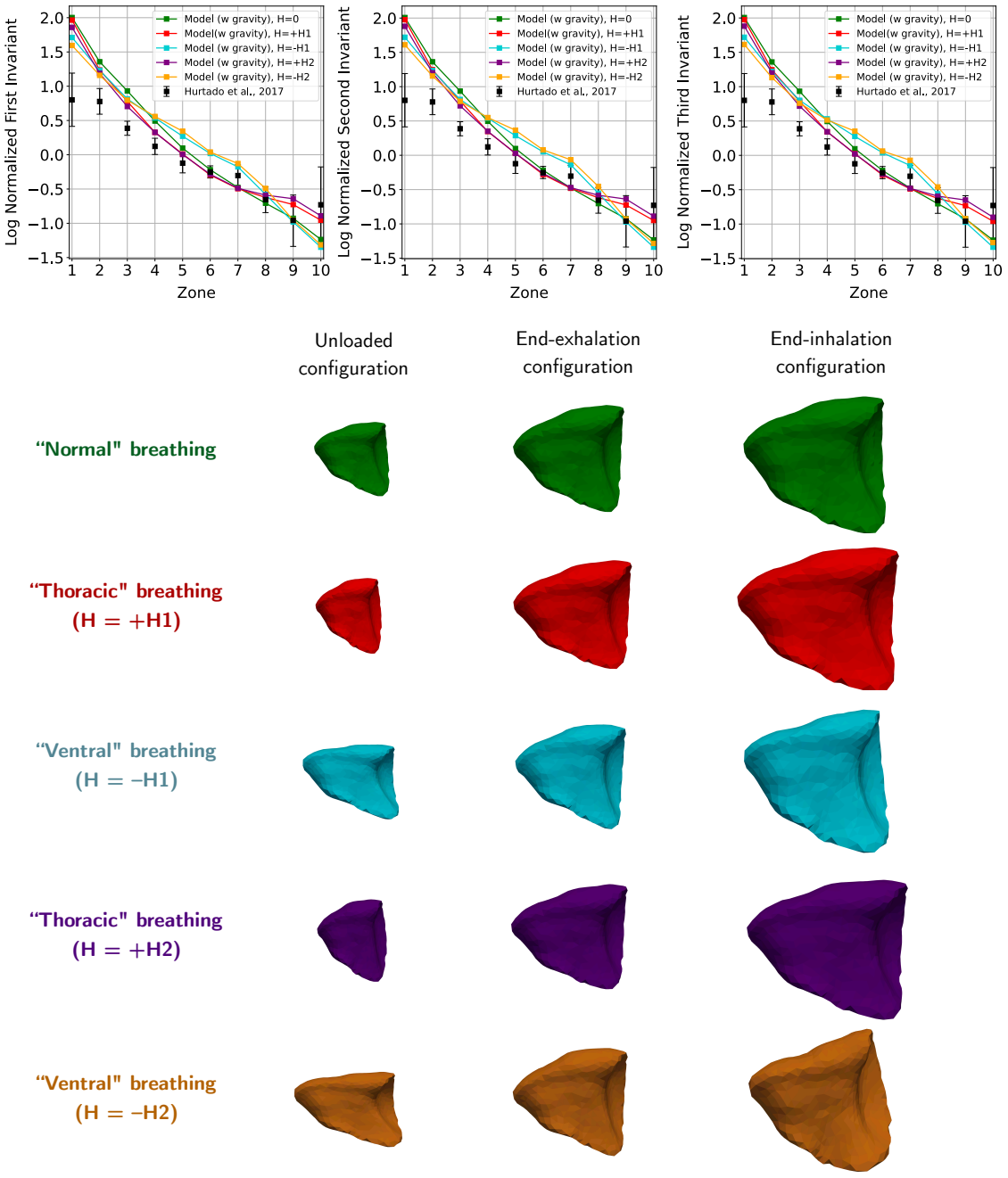

Figure 8: (a) Spatial distribution of the log-normal first invariant (left), second invariant (middle), and third invariant (right), for H = 0 (green curve), H = +0.005K (red curve), H = –0.005K (blue curve), H = +0.0065K (yellow curve) and H = –0.0065K (purple curve). Our results show that for the three invariants, the values are higher in the dorsal region, and decrease steadily until reaching their lowest value in the ventral region. Varying the reference pleural pressure also has an impact on the invariants distribution. (b) Illustration of the various steps of the calculation for the five cases.

lungs with the thoracic cage. We now compare this heterogeneity to the one obtained with our current model, which was just shown to be consistent with experimental observations.

Figure 9 presents the average values of the first, second and third invariants in each of the ten zones with our former model (green) and with our new formulation including gravity, in prone (red) and supine (blue) positions. Note that for the results obtained with our current model in prone and supine positions, the values of the parameters of material laws are chosen to be as close as possible to the parametrization used to obtain the results of [Patte, Genet, et al. 2022]; these values –presented in Table 1, with $\alpha = 0.16$kPa– are slightly different from the ones chosen to generate the data of Figure 8, so that values of the green curves of Figure 8 are different from the values of the curves for the supine position of Figure 9. Nevertheless, with our former model, the average value for the three invariants in every zone remain almost the same. Conversely, with our current model, in the supine position the values for each invariant is higher in the dorsal region and decrease until reaching their lowest value in the ventral region, and vice versa in the prone position.

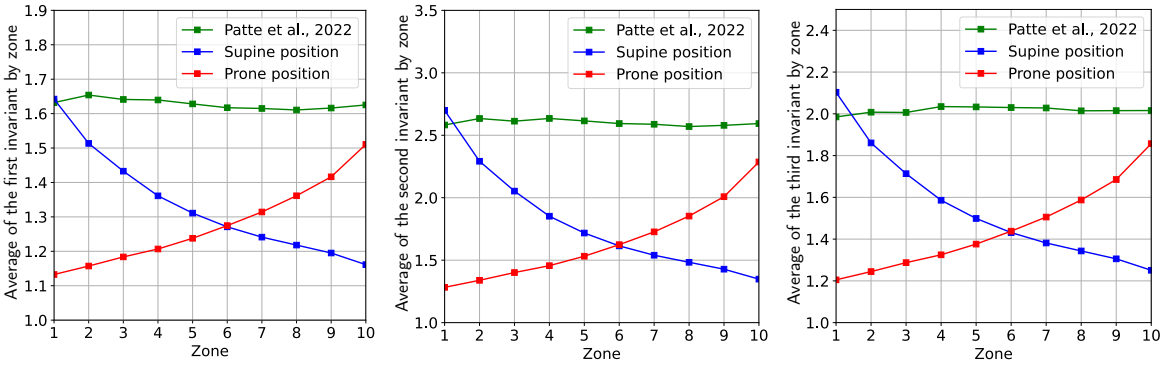

Figure 9: Spatial distribution of the first (left), second (center) and third (right) invariants with our former model and with our new formulation in prone and supine positions. In the former model, the average of the invariants remains roughly homogeneous in all zones, and does not vary in prone vs. supine position as there is no gravity in the model. With our new formulation, the strain invariants vary across the coronal zones, and the behavior in prone position differs greatly from the behavior in supine position.

4 Discussion

In the scope of this work, we assumed that gravity had a non negligible impact on the mechanical behavior of the lungs, and that it was partly responsible for the heterogeneity in breathing strain quantities of interest observed experimentally. We thus proposed a formulation of physiological boundary conditions allowing to take gravity into account. The results presented in this article seem to validate our initial hypothesis. We now discuss our results in details.

4.1 Computed pleural pressure distribution

The boundary conditions proposed in this paper lead to an heterogeneous pleural pressure applied onto the lungs, as presented in Figure 2, which corresponds to what is physiologically observed [Barrau et al. 2022]. At end-exhalation, the values of the pressure distribution range from –0.1 kPa to –1 kPa, which is consistent with data that can be found in literature, as presented in Table 3. The maximum and minimum values we find seem to correspond to the range of values presented in [Tawhai et al. 2009] and [Kallet 2015]. However, our gradient is higher: –0.9 kPa with our results, for a gradient of –0.5 kPa in [Kallet 2015] and of –0.7 kPa in [Tawhai et al. 2009]. If our gradient is almost twice the gradient presented in [Kallet 2015], the authors however highlighted that there could be approximations in the values presented, notably due to measurement techniques. This could explain their low pressure gradient value. It is also possible that the pleural

pressure gradient we obtain is higher than what was observed in [Tawhai et al. 2009] and [Kallet 2015] because of the parametrization of our model. The value of our pleural pressure depends indeed greatly on the expression of the reference pressure $\tilde{p}_{pl}$ implemented. The constants involved in the expression of $\tilde{p}_{pl}$ (see Equation (30)) are indeed fixed here at "normal" values that do not necessarily correspond to the data of a real patient. The values we chose could therefore explain why our gradient is higher than [Tawhai et al. 2009]. The value we obtain seems however reasonably close, especially considering that the pressure gradient varies greatly from one patient to another. It is therefore possible that the difference in the values we obtained is solely due to this high variability.

	Values from [Tawhai et al. 2009]	Values from [Kallet 2015]	Values from this paper
Min. value	–0.5 kPa	–0.1 kPa	–0.1 kPa
Max. value	–1.2 kPa	–0.6 kPa	–1.0 kPa

Table 3: Comparison of the values obtained for the porosity with values obtained in the literature.

We could not find data on the pleural pressure distribution at forced inspiration. The values we obtain seem however consistent, with a gradient of pleural pressure remaining similar to the value we obtained at end-exhalation (0.9 kPa). The form of the gradient is also consistent with what was described in [Barrau et al. 2022]: the value is more negative in the ventral region than in the dorsal region to balance gravity. When gravity is not taken into account, the pleural pressure of our model is uniform in the lungs. This is consistent with the studies of [Michels et al. 1978] and [Bryan et al. 1966], who suggested that under 0G, the expansion of the lungs should be uniform.

4.2 Model response

4.2.1 Global pressure-volume response

We assumed that gravity had an impact on the global and local response of the lungs. In terms of global response, we are particularly interested in the deformation and in the compliance of the lungs, from which biomarkers could be derived in the future. The compliance of the lungs is very dependent on the stiffness of the tissues, which can take a wide range of values, depending on the considered individual. We therefore studied the pressure-deformation response of the right lung, with and without gravity, for three different values of stiffnesses.

For the three values of stiffnesses studied, the results for the pressure-deformation curve are consistent with [Patte, Genet, et al. 2022]: the higher the stiffness, the lower the compliance of the lung. The impact of gravity on our generic lung also depends on the stiffness. For the highest stiffness, the behavior of the lung is very similar with or without gravity, with a relative difference between the two cases always under 0.6%. This could be expected, insofar as the stiffer the tissue, the higher a force needs to be to have an impact on the behavior of the structure. As a result, the impact of gravity is barely visible for the highest value of the stiffness. For lower stiffnesses, the impact of gravity on the pressure-volume response is more noticeable, especially for smaller values of pleural pressure. As could be expected, the lower the stiffness of the tissues, the higher the impact of gravity.

For physiological values of the end-inhalation pleural pressure (i.e., above 1 kPa), its impact can be considered to be much higher than the impact of gravity. The effect of gravity should therefore not be visible for end-inhalation pressures ranging form 1 kPa to 2 kPa. However, the actual end-inhalation and end-exhalation configurations are computed from the unloaded configuration, which is itself computed from the generic end-exhalation configuration. Since the end-exhalation pressure is not high enough to neglect gravity, the unloaded configuration is different with and without gravity, which leads to different end-inhalation configurations, even with high end-inhalation pressure values. Given the definition of our problem, the actual end-exhalation volumes (i.e., volumes of the end-exhalation state computed with the porosity changes described in the Methods section) are fairly close for all cases. This explains the difference observed in the Jacobian values with and without gravity.

The relative difference of the deformation with and without gravity does however not vary significantly for the range of end-inhalation pressure studied. This is consistent with the observations of [Sutherland et al. 1968], who hypothesized that the changes in lung compliance between 0G and normal gravity should be visible for low pressure values (close to the values at forced expiration), but not for typical values of the breathing cycle.

For the three cases studied, the Jacobian values are higher in the case without gravity than the case with gravity. This is consistent with the results obtained by [Bondurant 1958], where the authors showed that the compliance of the lungs decreased when the acceleration of gravity increased. [Bettinelli et al. 2002] also showed that the compliance of the lungs was higher under 0G, and smaller under normal gravity. Our results also seems consistent with our approach. Given our definition of the problem, the actual end-exhalation volume of the lungs is very close with and without gravity. At end-inhalation, however, the deformation of the lungs is higher when gravity is taken into account, with, in particular, more compression, which is consistent with the observations of [Seyfi Noferest et al. 2018]. Those deformations lead to a smaller end-inhalation volume, which explains the higher Jacobians without gravity.

4.2.2 Porosity distribution

Determining accurately the porosity field of our model is a key issue, since porosity has an impact on the behavior of the tissues, and therefore on the global and local response of the lungs. In terms of applications, this result confirms that, when building personalized models in the clinical setting, using patient-specific porosity fields, for instance extracted from clinical images, is critical to obtain physiologically relevant models.

More precisely, Figure 4 illustrates the impact of gravity on the porosity distribution computed at end-exhalation and at end-inhalation. Porosity increases compared to the unloaded configuration. This is due to the air flowing in the lungs. To compute the end-exhalation configuration from the unloaded configuration, the pleural pressure, which is negative, is applied onto the lung surface, causing air to flow within the lung. It hence causes an increase of the porosity.

Our results show a real impact of gravity on the porosity distribution, especially at end-exhalation. When no gravitational body force is applied, the pleural pressure is uniform (see Figure 2). It is therefore reasonable to expect the same profile for the distribution at end-exhalation as in the unloaded configuration. On the contrary, when gravity is taken into account, the porosity distribution is wider, and has a form closer to a Gaussian. This is due to the boundary conditions balancing gravity. Indeed, to balance gravity, the boundary pressure is higher (more negative) in the ventral region than in the dorsal region. With gravity, the dorsal part of the lungs is therefore in compression, which induces air to flow out. This results in a diminution of the fluid phase and hence of the porosity. Similarly, the pressure implemented as boundary condition induces tensile stresses in the ventral region to balance gravity. In this region, porosity therefore increases slightly. This phenomena explain the more heterogenous distribution of porosity at end-exhalation when taking gravity into account.

The impact of gravity on the porosity distribution is barely noticeable at end-inhalation. The distribution is indeed almost the same with or without taking gravity into account. At end-inhalation, the pleural pressure considered is six times higher than the pleural pressure considered at end-exhalation. It is therefore reasonable to consider that at end-inhalation the impact of gravity on the porosity distribution is negligible compared to the pleural pressure, which is visible on the porosity distribution.

The values we obtain at end-exhalation and end-inhalation fall within the range of porosities described in [DeGroot et al. 2018], where the average porosities considered are within 0.7 and 0.9. Our values are also close to the values of [Yang et al. 2020], presented in Table 4. In this study, the authors investigated the mean porosity for female and male patients during a full breathing cycle.

Our values are slightly higher than the values presented in [Yang et al. 2020]—about 15% of difference between our values and the values presented for females. However, their values are also

smaller than the values in [DeGroot et al. 2018]. This may result from the initial porosity chosen in this article, which was not detailed. The difference in porosity at end-inhalation can also be explained by the fact that the porosity they present in their work is measured during normal breathing, while the porosity we present in this study is at forced inhalation. The higher porosities in the dorsal area at end-exhalation are consistent with the results of [Gattinoni et al. 2023], who observed that the gas/tissue ratio was multiplied by 1.5 between the ventral area and the dorsal area.

	Female porosity from [Yang et al. 2020]	Male porosity from [Yang et al. 2020]	Mean porosity from this study
End-exhalation porosity	0.66	0.64	0.77
End-inhalation porosity	0.71	0.70	0.85

Table 4: Comparison of the values obtained for the end-exhalation pleural pressure with values obtained in the literature.

4.2.3 Strain distribution

In the results presented in Figure 5, we observe that the deformation is highly heterogeneous in the lung when gravity is taken into account. Both I_{1U}, I_{2U}, and J take higher values in the dorsal area when the patient is in supine position, which is consistent with results that have been observed in [Hurtado et al. 2017]. The deformations are globally higher in the dorsal region, which is also consistent with the observation of higher ventilation in the dorsal region for patients in supine position [West 2011].

[Tawhai et al. 2009] and [Gattinoni et al. 2023] also highlighted that the dorsal region was compressed and the ventral region more extended in supine position, which necessarily results in higher deformations between end-exhalation and end-inhalation in the dorsal region, the impact of gravity being less visible at end-inhalation than at end-exhalation. These observations are also supported by [Amelon et al. 2011], who highlighted that higher volume deformations should be expected in dorsal regions.

Gravity also induces shear stresses in the lungs, which are expected along the plane perpendicular to the application of gravity. The base being wider than the apex, higher deviatoric strains can be expected there. The localization of deviatoric strains at the base of the lungs could also resonate with the fact that IPF usually develops first at the base of the lungs and then spreads towards the apex.

When gravity is not taken into account, the deformations are homogeneous, which is consistent with observations of [Prisk 2014], who observed that ventilation and perfusion are heterogenous under normal gravity, but more homogeneous under 0G.

4.2.4 Stress distribution

Similarly, the maps of hydrostatic and deviatoric stresses display highly heterogeneous behaviors. The deviatoric and hydrostatic stresses are larger in the ventral part than in the dorsal part, as for the three reduced invariants. The distribution of the stresses is consistent with our proposed boundary conditions. Indeed, as a reaction to gravity, the pleural pressure is higher in the ventral region than in the dorsal region. The ventral region therefore experiences a higher tensile stress than the dorsal region, which explains the stress distribution.

4.3 Comparison with experimental data

Figure 8 shows that our results are very close to the data presented in [Hurtado et al. 2017], even though some details differ. In the results presented by [Hurtado et al. 2017], the value of the invariants increases between the ninth and the tenth region, while the values we present decrease. We assume it is due to the image registration process, in which the errors are typically higher close to the boundaries [Berberoğlu et al. 2021; Genet 2023]. Similarly, the values of our invariants

are significantly higher in the first region, which can partly be explained by the same phenomena. Moreover, the parametrization (parameter values chosen, form of the pleural pressure, etc.) also has an impact on the evolution of the invariants, which could explain the differences observed. However, our results seem to display the same overall behavior.

Little data is available in the literature on the regional deformation of the lungs during ventral and thoracic breathing. In this discussion, we will call non-specific breathing the breathing cycle that does not represent costal nor thoracic breathing (green curve). During thoracic (red and purple curves), the value of the invariants is smaller in the ventral and dorsal regions than for the non-specific breathing, and globally higher in the mid-part of the lung. This can be explained by the form of the expression of the thoracic breathing: the pressure is higher (i.e., less negative) in the mid-part of the lung and smaller (i.e., more negative) at the apex and the base. Since the absolute pressure is smaller in the mid-part of the lung, the deformation —length, surface and volume— can be expected to be smaller as well, which can explain the behavior of the curve.

Even though the curve for the costal breathing (blue and brown curves) is different from the non-specific breathing, it remains close to it. This is due to the form of the expression of costal breathing, where the pressure is higher (i.e., less negative) at the base and the apex of the lung than in its mid-part. The additional deformation introduced by the costal breathing can be approximated as a homogeneous deformation perpendicular to the direction of application of gravity. The variation of the invariants in each zone therefore remains almost solely due to gravity, which explains why the curve remains close to the non-specific breathing case. Nonetheless, these results indicate that by adapting the reference pleural pressure, we should be able to represent highly physiological boundary conditions with our model.

4.4 Comparison with our previous model

The implementation of gravity allows to take into account gravitational effects on the deformation of the lungs compared to our former model. In particular, this implementation allows to investigate various cases according to the orientation of gravity —-e.g., prone, supine or upright positions– . Figure 9 indeed shows that the deformation varies greatly according to the orientation of the patient, which could not be taken into account in our former model. As discussed earlier, the evolution of the invariants in supine position corresponds to data available in literature, which allows us to validate our results.

5 Conclusion and perspectives

In this work, we proposed the formulation of novel pressure boundary conditions for the lungs that balance gravity to verify the global equilibrium. This formulation is based on a constrained minimization problem. The boundary conditions we propose aim at incorporating gravity in our model, which has a non-negligible impact on the behavior of the lungs. It is however important to highlight that taking gravity into account in our model is only justified by the range of pleural pressure considered. Indeed, for larger pleural pressures, gravity would become negligible.

The formulation of our boundary conditions allowed us to study the impact of gravity on local and global quantities. In particular, we could reproduce the data of [Hurtado et al. 2017], which allows us to validate our data. We could also highlight the impact of gravity on various quantities, such as the local changes of dimensions —length, surface and volume— between end-exhalation and end-inhalation, the porosity, the pressure-volume response of the lungs, or the stress distribution.

We therefore achieved to formulate boundary conditions that remain physiological, and allow to include phenomena caused by gravity, which is not always straightforward in biomechanics. This is an important step forward in the improvement of our model. It indeed allows us to improves the physiological relevancy of our model.

A next step to improve this work would be to study the expression of the reference pleural pressure. Indeed, a simple expression for this pressure has been proposed in this article, but could

be improved. In particular, further investigations for taking properly into account diaphragmatic and costal breathing should be conducted in the future. Another step of improvement would be to include additional phenomena in our model, and to study their impact on the deformation of the lungs when gravity is considered. In particular, we would like to increase the physiological relevancy of our model by taking into account two fluid phases, air and blood, and one solid phase, the lung parenchyma (currently, the fluid phase corresponds to the air and the solid phase to the blood and lung parenchyma). Modeling the structural heterogeneities of the lungs, e.g., by incorporating the microstructure of the lungs and the airway tree in our macroscale model, would also improve the model and provide additional information on the impact of gravity on lung behavior, e.g., information on the impact of gravity on the deformation of the airway tree. Ultimately, we would like to apply this model to clinical data, and in particular to data of patients with IPF; this study could confirm whether gravity has an impact on patients presenting locally stiffer lung tissues.

Taking gravity into account in the model could also improve the personalization process in digital twin-based biomedical applications. Gravity could indeed be helpful to decrease model and estimation errors made during the identification of the parameters of our model [Patte, Genet, et al. 2022; Laville et al. 2023], by considering images both in prone and supine positions during the estimation process. Our boundary conditions are therefore a valuable improvement for the personalization of the model, which could eventually help build a digital twin of the lungs. These boundary conditions can be used in a wide variety of other lung models to improve their accuracy and/or to study the impact of gravity in diverse phenomena, such as mechanical ventilation for example [Sattari et al. 2023]. This could in particular help clinicians to improve patient care in various diseases, such as IPF.

Acknowledgements

We would like to thank Patrick Le Tallec for the discussions we had about the formulation of our boundary conditions. We would also like to thank the French National Research Agency (ANR) for providing financial support to this project (Grants no: ANR-19-CE45-0007 and ANR-20-COV4-0004).

References

Alnæs, M., J. Blechta, J. Hake, A. Johansson, B. Kehlet, A. Logg, C. Richardson, J. Ring, M. E. Rognes, and G. N. Wells (2015). "The FEniCS Project Version 1.5". In: *Archive of Numerical Software* Vol 3. DOI: 10.11588/ans.2015.100.20553.

Álvarez-Barrientos, F., D. E. Hurtado, and M. Genet (2021). "Pressure-Driven Micro-Poro-Mechanics: A Variational Framework for Modeling the Response of Porous Materials". In: *International Journal of Engineering Science* 169, p. 103586. DOI: 10.1016/j.ijengsci.2021.103586.

Amelon, R., K. Cao, K. Ding, G. E. Christensen, J. M. Reinhardt, and M. L. Raghavan (2011). "Three-dimensional characterization of regional lung deformation". In: *Journal of biomechanics* 44.13, pp. 2489–2495. DOI: 10.1016/j.jbiomech.2011.06.009.

Barrau, N., C. P. Barakat, Z. He, T. Emre, A. Nemeth, A. Afkir, W. Cai, V. Brulon, T. Boucneau, B. Fernandez, F. Besson, V. Lebon, and X. Maître (2022). "3D MR spirometry sensitivity to gravity lung dependence in healthy volunteers". In: *Conference presentation at ISMRT 31st annual meeting*. URL: https://archive.ismrm.org/2022/2064.html.

Baudet, V., P.-F. Villard, F. Jaillet, M. Beuve, and B. Shariat (2003). "Towards Accurate Tumour Tracking in Lungs." In: *Proceedings on Seventh International Conference on Information Visualization* 3, pp. 338–343. DOI: 10.1109/IV.2003.1218000.

Berberoğlu, E., C. T. Stoeck, P. Moireau, S. Kozerke, and M. Genet (2021). "In-silico study of accuracy and precision of left-ventricular strain quantification from 3D tagged MRI". In: *PloS one* 16.11, e0258965. DOI: 10.1371/journal.pone.0258965.

Berger, L., R. Bordas, K. Burrowes, V. Grau, S. Tavener, and D. Kay (2016). "A poroelastic model coupled to a fluid network with applications in lung modelling". In: *International journal for numerical methods in biomedical engineering* 32.1. DOI: 10.1002/cnm.2731.

Bettinelli, D., C. Kays, O. Bailliart, A. Capderou, P. Techoueyres, J.-L. Lachaud, P. Vaida, and G. Miserocchi (2002). "Effect of gravity and posture on lung mechanics". In: *Journal of applied physiology* 93.6, pp. 2044–2052. DOI: 10.1152/japplphysiol.00492.2002.

Bondurant, S. (1958). "Effect of acceleration on pulmonary compliance". In: *Federation Proceedings*. Vol. 17. 1, pp. 18–18.

Boucneau, T., B. Fernandez, P. Larson, L. Darrasse, and X. Maître (2020). "3D Magnetic Resonance Spirometry". In: *Scientific Reports* 10.1, p. 9649. DOI: 10.1038/s41598-020-66202-7.

Bryan, A., J. Milic-Emili, and D. Pengelly (1966). "Effect of gravity on the distribution of pulmonary ventilation." In: *Journal of Applied Physiology* 21.3, pp. 778–784. DOI: 10.1152/jappl.1966.21.3.778.

Carniel, E., I. Toniolo, and C. G. Fontanella (2020). "Computational Biomechanics: In-Silico Tools for the Investigation of Surgical Procedures and Devices". In: *Bioengineering* 7, p. 48. DOI: 10.3390/bioengineering7020048.

Caruel, M., R. Chabiniok, P. Moireau, Y. Lecarpentier, and D. Chapelle (2014). "Dimensional reductions of a cardiac model for effective validation and calibration". In: *Biomechanics and modeling in mechanobiology* 13, pp. 897–914. DOI: 10.1007/s10237-013-0544-6.

Chabiniok, R., P. Moireau, P.-F. Lesault, A. Rahmouni, J.-F. Deux, and D. Chapelle (2012). "Estimation of tissue contractility from cardiac cine-MRI using a biomechanical heart model". In: *Biomechanics and modeling in mechanobiology* 11, pp. 609–630. DOI: 10.1007/s10237-011-0337-8.

Chabiniok, R., V. Y. Wang, M. Hadjicharalambous, L. Asner, J. Lee, M. Sermesant, E. Kuhl, A. A. Young, P. Moireau, M. P. Nash, D. Chapelle, and D. A. Nordsletten (2016). "Multiphysics and Multiscale Modelling, Data–Model Fusion and Integration of Organ Physiology in the Clinic: Ventricular Cardiac Mechanics". In: *Interface Focus* 6.2, p. 20150083. DOI: 10.1098/rsfs.2015.0083.

Chapelle, D. and P. Moireau (2014). "General coupling of porous flows and hyperelastic formulations—from thermodynamics principles to energy balance and compatible time schemes". In: *European Journal of Mechanics-B/Fluids* 46, pp. 82–96. DOI: 10.1016/j.euromechflu.2014.02.009.

Cottin, V., P. Bonniaud, J. Cadranel, B. Crestani, S. Jouneau, S. Marchand-Adam, H. Nunes, L. Wémeau-Stervinou, E. Bergot, E. Blanchard, et al. (2022). "Recommandations pratiques pour le diagnostic et la prise en charge de la fibrose pulmonaire idiopathique–Actualisation 2021, version intégrale". In: *Revue des Maladies Respiratoires* 39.7, e35–e106. DOI: 10.1016/j.rmr.2017.07.017.

Coussy, O. (2004). *Poromechanics*. John Wiley & Sons.

DeGroot, C. T. and A. G. Straatman (2018). "A porous media model of alveolar duct flow in the human lung". In: *Journal of Porous Media* 21.5. DOI: 10.1615/JPorMedia.v21.i5.20.

Demiray, H. (1972). "A note on the elasticity of soft biological tissues". In: *Journal of biomechanics* 5.3, pp. 309–311. DOI: 10.1016/0021-9290(72)90047-4.

Fuerst, B., T. Mansi, F. Carnis, M. Sälzle, J. Zhang, J. Declerck, T. Boettger, J. Bayouth, N. Navab, and A. Kamen (2014). "Patient-specific biomechanical model for the prediction of lung motion from 4-D CT images". In: *IEEE transactions on medical imaging* 34.2, pp. 599–607. DOI: 10.1109/TMI.2014.2363611.

Galvin, I., G. Drummond, and M. Nirmalan (2007). "Distribution of blood flow and ventilation in the lung: gravity is not the only factor". In: *British journal of anaesthesia* 98.4, pp. 420–428. DOI: 10.1093/bja/aem036.

Ganesan, S., K. E. Rouch, and S. J. Lai-Fook (1995). "A finite element analysis of the effects of the abdomen on regional lung expansion". In: *Respiration physiology* 99.3, pp. 341–353. DOI: 10.1016/0034-5687(94)00104-8.

Gattinoni, L., S. Brusatori, R. D'Albo, R. Maj, M. Velati, C. Zinnato, S. Gattarello, F. Lombardo, I. Fratti, F. Romitti, et al. (2023). "Prone position: how understanding and clinical application of a technique progress with time". In: *Anesthesiology and Perioperative Science* 1.1, p. 3. DOI: 10.1007/s44254-022-00002-2.

Genet, M. (2023). "Finite strain formulation of the discrete equilibrium gap principle: I-mechanically consistent regularization for large motion tracking". In: *Preprint*.

Genet, M., L. Chuan Lee, L. Ge, G. Acevedo-Bolton, N. Jeung, A. Martin, N. Cambronero, A. Boyle, Y. Yeghiazarians, S. Kozerke, and J. M. Guccione (2015). "A novel method for quantifying smooth regional variations in myocardial contractility within an infarcted human left ventricle based on delay-enhanced magnetic resonance imaging". In: *Journal of biomechanical engineering* 137.8, p. 081009. DOI: 10.1115/1.4030667.

Genet, M., L. C. Lee, B. Baillargeon, J. M. Guccione, and E. Kuhl (2016). "Modeling pathologies of diastolic and systolic heart failure". In: *Annals of biomedical engineering* 44, pp. 112–127. DOI: 10.1007/s10439-015-1351-2.

Genet, M., L. C. Lee, R. Nguyen, H. Haraldsson, G. Acevedo-Bolton, Z. Zhang, L. Ge, K. Ordovas, S. Kozerke, and J. M. Guccione (2014). "Distribution of normal human left ventricular myofiber stress at end diastole and end systole: a target for in silico design of heart failure treatments". In: *Journal of applied physiology* 117.2, pp. 142–152. DOI: 10.1152/japplphysiol.00255.2014.

Genet, M., C. Patte, C. Fetita, P.-Y. Brillet, and D. Chapelle (2020). "Personalized pulmonary poromechanics". In: *Computer Methods in Biomechanics and Biomedical Engineering* 23.sup1, S119–S120. DOI: 10.1080/10255842.2020.1812842.

Genet, M., C. Patte, M. Manoochehrtayebi, and A. Peyraut (2024). *Dolfin_mech*. URL: https://doi.org/10.5281/zenodo.8010870.

Gindre, J., A. Bel-Brunon, M. Rochette, A. Lucas, A. Kaladji, P. Haigron, and A. Combescure (2016). "Patient-specific finite-element simulation of the insertion of guidewire during an EVAR procedure: guidewire position prediction validation on 28 cases". In: *IEEE Transactions on Biomedical Engineering* 64.5, pp. 1057–1066. DOI: 10.1109/TBME.2016.2587362.

Glaister, D., M. Ironmonger, and B. Lisher (1975). *The effect of transversely applied acceleration on lung mechanics in man*. RAF Institute of Aviation Medicine.

Han, L., H. Dong, J. R. McClelland, L. Han, D. J. Hawkes, and D. C. Barratt (2017). "A hybrid patient-specific biomechanical model based image registration method for the motion estimation of lungs". In: *Medical image analysis* 39, pp. 87–100. DOI: 10.1016/j.media.2017.04.003.

Himanshu, K. (2019). "Respiratory healthcare by design: computational approaches bringing respiratory precision and personalised medicine closer to bedside". In: *Morphologie* 103 (343), pp. 194–202. DOI: 10.1016/j.morpho.2019.10.042.

Hinz, B. and B. Suki (2016). "Does breathing amplify fibrosis?" In: *American journal of respiratory and critical care medicine* 194.1, pp. 9–11. DOI: 10.1164/rccm.201601-0149ED.

Hurtado, D. E., N. Villarroel, C. Andrade, J. Retamal, G. Bugedo, and A. Bruhn (2017). "Spatial patterns and frequency distributions of regional deformation in the healthy human lung". In: *Biomechanics and modeling in mechanobiology* 16, pp. 1413–1423. DOI: 10.1007/s10237-017-0895-5.

Hutchinson, J., A. Fogarty, R. Hubbard, and T. McKeever (2015). "Global incidence and mortality of idiopathic pulmonary fibrosis: a systematic review". In: *European Respiratory Journal* 46.3, pp. 795–806. DOI: 10.1183/09031936.00185114.

Kallet, R. H. (2015). "A comprehensive review of prone position in ARDS". In: *Respiratory care* 60.11, pp. 1660–1687. DOI: 10.4187/respcare.04271.

Kaneko, K., J. Milic-Emili, M. Dolovich, A. Dawson, and D. Bates (1966). "Regional distribution of ventilation and perfusion as a function of body position." In: *Journal of Applied Physiology* 21.3, pp. 767–777. DOI: 10.1152/jappl.1966.21.3.767.

Kumaresan, A., R. Gerber, A. Mueller, S. H. Loring, and D. Talmor (2018). "Effects of prone positioning on transpulmonary pressures and end-expiratory volumes in patients without lung disease". In: *Anesthesiology* 128.6, pp. 1187–1192. DOI: 10.1097/ALN.0000000000002159.

Kyriakou, E. and D. McKenzie (2011). "Dynamic modeling of lung tumor motion during respiration". In: *Physics in Medicine & Biology* 56.10, p. 2999. DOI: 10.1088/0031-9155/56/10/007.

Laville, C., C. Fetita, T. Gille, P.-Y. Brillet, H. Nunes, J.-F. Bernaudin, and M. Genet (2023). "Comparison of optimization parametrizations for regional lung compliance estimation using personalized pulmonary poromechanical modeling". In: *Biomechanics and Modeling in Mechanobiology*, pp. 1–13. DOI: 10.1007/s10237-023-01691-9.

Lee, L. C., M. Genet, A. B. Dang, L. Ge, J. M. Guccione, and M. B. Ratcliffe (2014). "Applications of computational modeling in cardiac surgery". In: *Journal of Cardiac Surgery: Including Mechanical and Biological Support for the Heart and Lungs* 29.3, pp. 293–302. DOI: 10.1111/jocs.12332.

Lee, Y. K., Y.-M. Oh, J.-H. Lee, E. K. Kim, J. H. Lee, N. Kim, J. B. Seo, S. D. Lee, and K. S. Group (2008). "Quantitative assessment of emphysema, air trapping, and airway thickening on computed tomography". In: *Lung* 186, pp. 157–165. DOI: https://doi.org/10.1007/s00408-008-9071-0.

Liu, F., J. D. Mih, B. S. Shea, A. T. Kho, A. S. Sharif, A. M. Tager, and D. J. Tschumperlin (2010). "Feedback amplification of fibrosis through matrix stiffening and COX-2 suppression". In: *Journal of Cell Biology* 190.4, pp. 693–706. DOI: 10.1083/jcb.201004082.

Logg, A., K.-A. Mardal, and G. Wells, eds. (2012). *Automated Solution of Differential Equations by the Finite Element Method: The FEniCS Book*. Lecture Notes in Computational Science and Engineering 84. Heidelberg: Springer. 723 pp.

Manoochehrtayebi, M., A. Bel-Brunon, and M. Genet (2023). "Finite strain micro-poro-mechanics: formulation and compared analysis with macro-poro-mechanics". In: *Journal of the Mechanics and Physics of Solids (Submitted)*.

McKleroy, W., T.-H. Lee, and K. Atabai (2013). "Always cleave up your mess: targeting collagen degradation to treat tissue fibrosis". In: *American Journal of Physiology-Lung Cellular and Molecular Physiology* 304.11, pp. L709–L721. DOI: 10.1152/ajplung.00418.2012.

Mentzer, S. J., A. Tsuda, and S. H. Loring (2018). "Pleural mechanics and the pathophysiology of air leaks". In: *The Journal of thoracic and cardiovascular surgery* 155.5, pp. 2182–2189. DOI: 10.1016/j.jtcvs.2017.12.062.

Michels, D. B. and J. B. West (1978). "Distribution of pulmonary ventilation and perfusion during short periods of weightlessness". In: *Journal of Applied Physiology* 45.6, pp. 987–998. DOI: 10.1152/jappl.1978.45.6.987.

Moireau, P., N. Xiao, M. Astorino, C. A. Figueroa, D. Chapelle, C. A. Taylor, and J.-F. Gerbeau (2012). "External tissue support and fluid–structure simulation in blood flows". In: *Biomechanics and modeling in mechanobiology* 11, pp. 1–18. DOI: 10.1007/s10237-011-0289-z.

Nalysnyk, L., J. Cid-Ruzafa, P. Rotella, and D. Esser (2012). "Incidence and prevalence of idiopathic pulmonary fibrosis: review of the literature". In: *European Respiratory Review* 21.126, pp. 355–361. DOI: 10.1183/09059180.00002512.

Neelakantan, S., Y. Xin, D. P. Gaver, M. Cereda, R. Rizi, B. J. Smith, and R. Avazmohammadi (2022). "Computational lung modelling in respiratory medicine". In: *Journal of The Royal Society Interface* 19.191, p. 20220062. DOI: 10.1098/rsif.2022.0062.

Nelson, T., K. Quiros, E. Dominguez, A. Ulu, T. Nordgren, and M. Eskandari (2023). "Diseased and healthy murine local lung strains evaluated using digital image correlation". In: *Scientific Reports* 13.1, p. 4564. DOI: 10.1038/s41598-023-31345-w.

Patte, C. (2020). "Personalized pulmonary mechanics: modeling, estimation and application to pulmonary fibrosis". PhD thesis. Institut polytechnique de Paris. URL: https://theses.hal.science/tel-03144413.

Patte, C., P.-Y. Brillet, C. Fetita, J.-F. Bernaudin, T. Gille, H. Nunes, D. Chapelle, and M. Genet (2022). "Estimation of regional pulmonary compliance in idiopathic pulmonary fibrosis based on personalized lung poromechanical modeling". In: *Journal of Biomechanical Engineering* 144.9, p. 091008. DOI: 10.1115/1.4054106.

Patte, C., M. Genet, and D. Chapelle (2022). "A quasi-static poromechanical model of the lungs". In: *Biomechanics and Modeling in Mechanobiology* 21.2, pp. 527–551. DOI: 10.1007/s10237-021-01547-0.

Peyraut, A. and M. Genet (2024). *Gravity modeling paper demos*. URL: https://doi.org/10.5281/zenodo.10521966.

Pfaller, M. R., M. Cruz Varona, J. Lang, C. Bertoglio, and W. A. Wall (2020). "Using parametric model order reduction for inverse analysis of large nonlinear cardiac simulations". In: *International journal for numerical methods in biomedical engineering* 36.4, e3320. DOI: 10.1002/cnm.3320.

Plantier, L., A. Cazes, A.-T. Dinh-Xuan, C. Bancal, S. Marchand-Adam, and B. Crestani (2018). "Physiology of the lung in idiopathic pulmonary fibrosis". In: *European Respiratory Review* 27.147. DOI: 10.1183/16000617.0062-2017.

Prisk, G. K. (2014). "Microgravity and the respiratory system". In: *European Respiratory Journal* 43.5, pp. 1459–1471. DOI: 10.1183/09031936.00001414.

San Bok, J., G. D. Lee, D. K. Kim, D. Lim, S. K. Joo, and S. Choi (2018). "Changes of pleural pressure after thoracic surgery". In: *Journal of Thoracic Disease* 10.7, p. 4109. DOI: 10.21037/jtd.2018.06.131.

Sattari, S., C. A. Mariano, W. G. Kuschner, H. Taheri, J. H. Bates, and M. Eskandari (2023). "Positive-and negative-pressure ventilation characterized by local and global pulmonary mechanics". In: *American Journal of Respiratory and Critical Care Medicine* 207.5, pp. 577–586. DOI: https://doi.org/10.1164/rccm.202111-2480OC.

Seyfi Noferest, B., A. P. Santhanam, and O. J. Ilegbusi (2018). "Effect of gravity on subject-specific human lung deformation". In: *Mathematical and Computer Modelling of Dynamical Systems* 24.1, pp. 87–101. DOI: 10.1080/13873954.2017.1382537.

Smit, H. J., R. P. Golding, F. M. Schramel, W. L. Devillé, R. A. Manoliu, and P. E. Postmus (2004). "Lung density measurements in spontaneous pneumothorax demonstrate airtrapping". In: *Chest* 125.6, pp. 2083–2090. DOI: 10.1378/chest.125.6.2083.

Smith, N. P., A. de Vecchi, M. McCormick, D. A. Nordsletten, O. Camara, A. F. Frangi, H. Delingette, M. Sermesant, J. Relan, N. Ayache, M. W. Krueger, W. H. W. Schulze, R. Hose, I. Valverde, P. Beerbaum, C. Staicu, M. Siebes, J. Spaan, P. J. Hunter, J. Weese, H. Lehmann, D. Chapelle, and R. Rezavi (2011). "euHeart: Personalized and Integrated Cardiac Care Using Patient-Specific Cardiovascular Modelling". In: *Interface focus* 1.3, pp. 349–64. DOI: 10.1098/rsfs.2010.0048.

Spagnolo, P., A. Tzouvelekis, and F. Bonella (2018). "The management of patients with idiopathic pulmonary fibrosis". In: *Frontiers in medicine* 5, p. 148. DOI: 10.3389/fmed.2018.00148.

Sutherland, P., T. Katsura, and J. Milic-Emili (1968). "Previous volume history of the lung and regional distribution of gas." In: *Journal of Applied Physiology* 25.5, pp. 566–574. DOI: 10.1152/jappl.1968.25.5.566.

Swigris, J., W. Kuschner, S. Jacobs, S. Wilson, and M. Gould (2005). "Health-related quality of life in patients with idiopathic pulmonary fibrosis: a systematic review". In: *Thorax* 60.7, pp. 588–594. DOI: 10.1136/thx.2004.035220.

Tawhai, M. H., M. P. Nash, C.-L. Lin, and E. A. Hoffman (2009). "Supine and prone differences in regional lung density and pleural pressure gradients in the human lung with constant shape". In: *Journal of Applied Physiology* 107.3, pp. 912–920. DOI: 10.1152/japplphysiol.00324.2009.

Vy, P., V. Auffret, P. Badel, M. Rochette, H. Le Breton, P. Haigron, and S. Avril (2016). "Review of patient-specific simulations of transcatheter aortic valve implantation". In: *International Journal of Advances in Engineering Sciences and Applied Mathematics* 8.1, pp. 2–24. DOI: 10.1007/s12572-015-0139-9.

Wells, A. U. (2018). "IPF diagnosis: flexibility is a virtue". In: *The Lancet Respiratory Medicine* 6.10, pp. 735–737. DOI: 10.1016/S2213-2600(18)30374-6.

Werner, R., J. Ehrhardt, R. Schmidt, and H. Handels (2009). "Patient-specific finite element modeling of respiratory lung motion using 4D CT image data". In: *Medical physics* 36.5, pp. 1500–1511. DOI: 10.1118/1.3101820.

West, J. B. (2011). "A Web-based course of lectures in respiratory physiology". In: *Advances in physiology education* 35.3, pp. 249–251. DOI: 10.1152/advan.00042.2011.

West, J. B. and F. L. Matthews (1972). "Stresses, strains, and surface pressures in the lung caused by its weight". In: *Journal of Applied Physiology* 32.3, pp. 332–345. DOI: 10.1152/jappl.1972.32.3.332.

Wijsenbeek, M. and V. Cottin (2020). "Spectrum of fibrotic lung diseases". In: *New England Journal of Medicine* 383.10, pp. 958–968. DOI: 10.1056/NEJMra2005230.

Wu, H., Y. Yu, H. Huang, Y. Hu, S. Fu, Z. Wang, M. Shi, X. Zhao, J. Yuan, J. Li, W. Yang, E. Bin, D. Wei, H. Zhang, J. Zhang, C. Yang, T. Cai, H. Dai, J. Chen, and N. Tang (2020). "Progressive pulmonary fibrosis is caused by elevated mechanical tension on alveolar stem cells". In: *Cell* 180.1, pp. 107–121. DOI: 10.1016/j.cell.2019.11.027.

Yang, D. and M. Cao (2020). "Effect of changes in lung physical properties on microwave ablation zone during respiration". In: *Biomedical Engineering Letters* 10, pp. 285–298. DOI: 10.1007/s13534-019-00145-5.

Zhang, T., N. P. Orton, T. R. Mackie, and B. R. Paliwal (2004). "A novel boundary condition using contact elements for finite element based deformable image registration". In: *Medical physics* 31.9, pp. 2412–2415. DOI: 10.1118/1.1774131.

A Impact of porosity distribution width and mesh size

A.1 Impact of porosity distribution width

In this appendix, we propose an additional study of the impact of a wider porosity distribution in the unloaded configuration ([0.3, 0.7]) on the porosity distribution at end-exhalation and end-inhalation, with and without gravity, presented in Figure A.1.

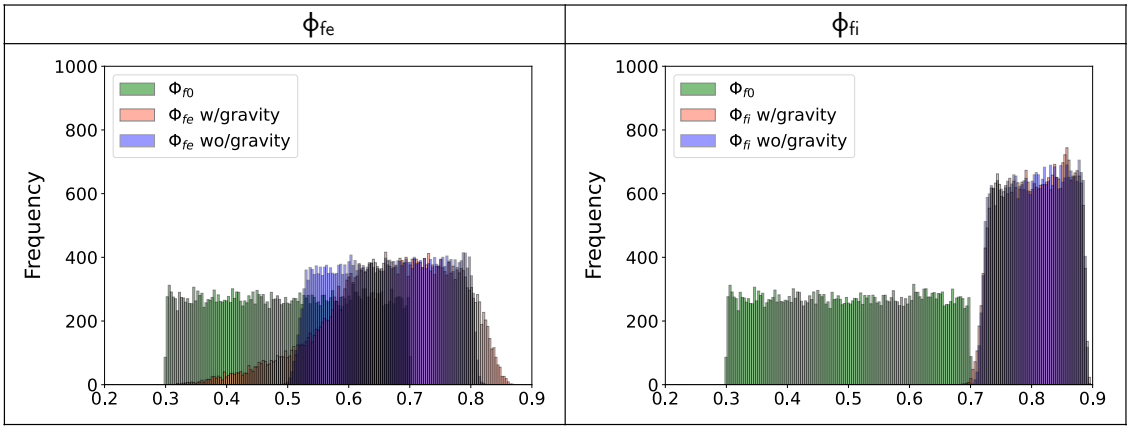

Figure A.1: Porosity distribution at end-exhalation (left) and at end-inhalation (right) for a porosity in the unloaded configuration following a uniform law ranging from 0.3 to 0.7.

The trends remain similar to what was observed in 4, but with wider distributions. The distribution are centered on the same values as before, but range from 0.4 to 0.9 at end-exhalation with gravity and 0.6 to 0.85 without gravity. At end-inhalation the porosity range from 0.72 to 0.9. The form of the distributions therefore remains the same as before, even though they take values in a wider range.

A.2 Impact of mesh size

We also include a brief convergence study of porosity distribution at end-exhalation and end-inhalation, with and without gravity, presented in Figure A.2. The results obtained in Figure 4 are compared with results for a finer mesh (approximately 10 times as many elements). The distribution remains the same; the number of elements do not have an impact on the results.

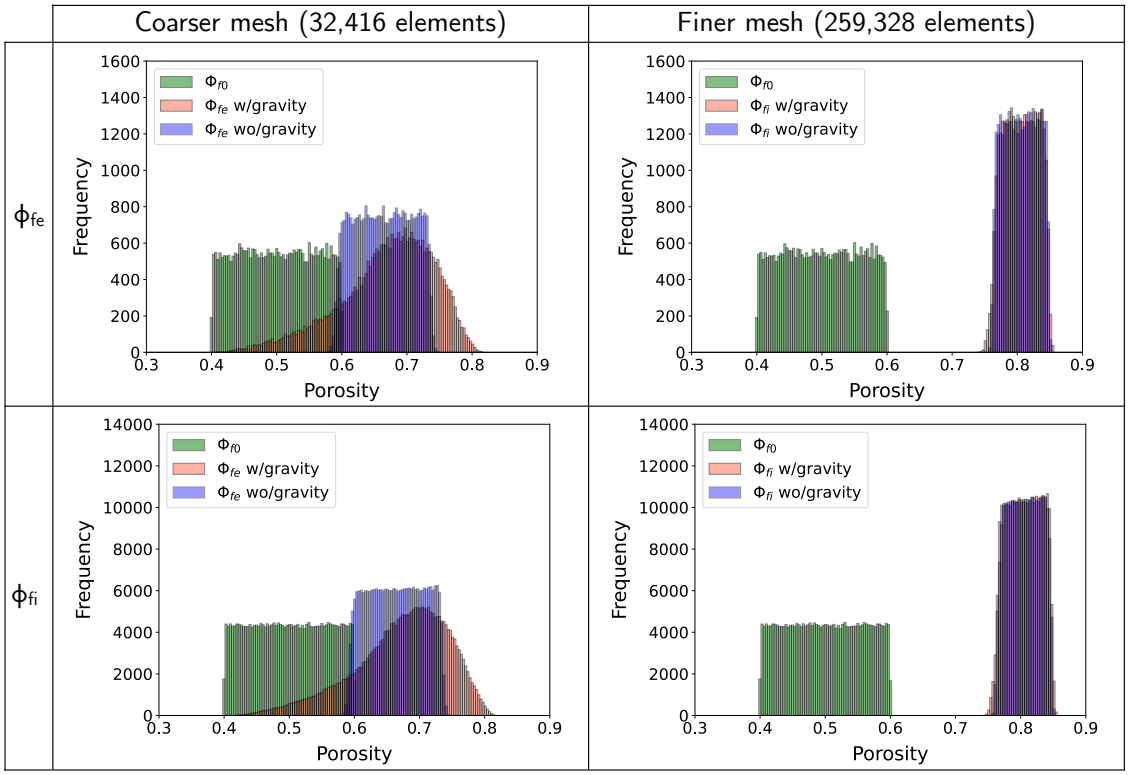

Figure A.2: Porosity distribution at end-exhalation (first row) and at end-inhalation (second row) for the mesh used in this article (left) and a finer mesh (right). The distribution is the same in the two cases. The results we obtained are converged.

B Code for Figure 3

Imports

[ ]:
```
import matplotlib.pyplot as plt
import pandas

import dolfin_mech as dmech
```

Parameters

Mesh

[ ]:
```
cube_params = {"path_and_mesh_name":"Data/generic_mesh.xdmf"}
```

Material

[ ]:
```
alpha_lst = [0.016, 0.16, 1.6] # kPa
params = {
    "alpha":0.16,      # kPa
    "gamma":0.5,       # [-]
    "c1":0.2,          # kPa
    "c2":0.4,          # kPa
    "kappa":1e2,       # kPa
    "eta":1e-5,        # kPa
    "rho_solid":1e-6} # g/mm3
mat_params = {"scaling":"linear", "parameters":params}
```

Loading

[ ]:
```
pe = -0.5    # kPa
pi = -2.0    # kPa
g  = +9.81e3 # mm/s2
```

Computing pressure-volume responses

[ ]:
```
results = {}
gravity_lst = [0,1]
for gravity_ in gravity_lst:
 for alpha_   in alpha_lst  :

    mat_params["parameters"]["alpha"] = alpha_

    ### computing the unloaded configuration from a generic end-exhalation configuration
    U_exhal_to_unloaded, phis_unloaded, dV_exhal = dmech.
 ↪run_RivlinCube_PoroHyperelasticity(
        inverse=1,
        cube_params=cube_params,
        porosity_params={"type":"mesh_function_random_xml", "val":0.3},
        # porosity_params={"type":"constant", "val":0.3},
        mat_params=mat_params,
        inertia_params={"applied":True, "rho_val":1e-8},
        step_params={"dt_min":1e-4, "dt_ini":0.125},
        load_params={"type":"p_boundary_condition0", "f":gravity_*g, "P0":float(pe)},
        res_basename="Fig3-unloaded"+str(alpha_)+str(gravity_),
        get_results=1,
        verbose=1)

    ### computing the end-exhalation configuration
```

```
   U_unloaded_to_exhal, phis_exhal, dV_unloaded = dmech.
↪run_RivlinCube_PoroHyperelasticity(
       cube_params=cube_params,
       move_params={"move":True, "U":U_exhal_to_unloaded},
       porosity_params={"type":"mesh_function_random_xml", "val":0.5},
       mat_params=mat_params,
       inertia_params={"applied":True, "rho_val":1e-8},
       step_params={"dt_ini":0.05, "dt_max":0.05, "dt_min":1e-4},
       load_params={"type":"p_boundary_condition", "f":gravity_*g, "P0":float(pe)},
       res_basename="Fig3-direct-exhal"+str(alpha_)+str(gravity_),
       get_results=1,
       verbose=1)

   ### computing the end-inhalation configuration
   U_unloaded_to_inhal, phis_inhal, dV_unloaded = dmech.
↪run_RivlinCube_PoroHyperelasticity(
       cube_params=cube_params,
       move_params={"move":True, "U":U_exhal_to_unloaded},
       porosity_params={"type":"mesh_function_random_xml", "val":0.5},
       mat_params=mat_params,
       inertia_params={"applied":True, "rho_val":1e-8},
       step_params={"n_steps":2, "Deltat":1., "dt_ini":0.05, "dt_max":0.05, "dt_min":
↪1e-4},
       load_params={"type":"p_boundary_condition", "f_lst":[gravity_*g, gravity_*g],␣
↪"P0_lst":[float(0.), float(pi)]},
       res_basename="Fig3-direct-inhal"+str(alpha_)+str(gravity_),
       get_results=1,
       verbose=1)

   v_lst = pandas.read_csv(
       "Fig3-direct-inhal"+str(alpha_)+str(gravity_)+"-qois.dat",
       delim_whitespace=True,
       comment="#",
       names=open("Fig3-direct-inhal"+str(alpha_)+str(gravity_)+"-qois.dat").
↪readline()[1:].split()).to_dict('list')["v"]

   V_exhal = pandas.read_csv(
       "Fig3-direct-exhal"+str(alpha_)+str(gravity_)+"-qois.dat",
       delim_whitespace=True,
       comment="#",
       names=open("Fig3-direct-exhal"+str(alpha_)+str(gravity_)+"-qois.dat").
↪readline()[1:].split()).to_dict('list')["v"][-1]

   t_lst = pandas.read_csv(
       "Fig3-direct-inhal"+str(alpha_)+str(gravity_)+"-qois.dat",
       delim_whitespace=True,
       comment="#",
       names=open("Fig3-direct-inhal"+str(alpha_)+str(gravity_)+"-qois.dat").
↪readline()[1:].split()).to_dict('list')["t"]

   results["pi_alpha="+str(alpha_)+"g="+str(gravity_)] = [-1*(2*t-1)*float(pi) for t in␣
↪t_lst if t>=0.5]
   results["J_alpha="+str(alpha_)+"g="+str(gravity_)] = [v_lst[c]/V_exhal for c in␣
↪range(len(t_lst)) if t_lst[c]>=0.5]
```

Generating plots

[ ]:
```
fig, ax = plt.subplots()

### plotting parameters
plt.rc("xtick", labelsize=14)
plt.rc("ytick", labelsize=14)
plt.rc("legend", fontsize=12)
plt.xlim([0.5, 2])
plt.ylim([0.9, 2.2])
fig.set_size_inches(8, 6)
plt.xlabel("End-inhalation pleural presure", fontsize=10)
plt.ylabel("Jacobian from end-exhalation to end-inhalation", fontsize=10)
color_lst = ["blue", "green", "orange"]

### curves
for alpha_ in alpha_lst:
    for gravity_ in gravity_lst:
        if gravity_:
            linestyle = "-"
            g = "w/ gravity"
        else:
            linestyle = "--"
            g = "w/o gravity"
        plt.plot(results["pi_alpha="+str(alpha_)+"g="+str(gravity_)],␣
 ↪results["J_alpha="+str(alpha_)+"g="+str(gravity_)], color=color_lst[0],␣
 ↪linestyle=linestyle, label=r"$\alpha$"+"="+str(alpha_)+" kPa, "+str(g))
    color_lst=color_lst[1:]

plt.legend()
plt.grid()
plt.show()
```

C Code for Figure 4

Imports

[ ]:
```
import copy
import matplotlib.pyplot as plt
import numpy

import dolfin_mech as dmech
```

Parameters

Mesh

[ ]:
```
cube_params = {"path_and_mesh_name":"Data/generic_mesh.xdmf", "refine":True} # the mesh is refined only for plotting purposes
```

Material

[ ]:
```
params = {
    "alpha":0.16,      # kPa
    "gamma":0.5,       # [-]
    "c1":0.2,          # kPa
    "c2":0.4,          # kPa
    "kappa":1e2,       # kPa
    "eta":1e-5,        # kPa
    "rho_solid":1e-6} # g/mm3
mat_params = {"scaling":"linear", "parameters":params}
```

Loading

[ ]:
```
pe = -0.5    # kPa
pi = -2.0    # kPa
g  = +9.81e3 # mm/s2
```

Computing porosity distributions

[ ]:
```
gravity_lst = [0,1]
for gravity_ in gravity_lst:

    ### computing the unloaded configuration from a generic end-exhalation configuration
    Uref, phisref_computation, dVexpiini = dmech.run_RivlinCube_PoroHyperelasticity(
        inverse=1,
        cube_params=cube_params,
        mat_params=mat_params,
        porosity_params={"type":"mesh_function_random_xml", "val":0.3},
        inertia_params={"applied":True, "rho_val":1e-8},
        step_params={"dt_min":1e-4, "dt_ini":1},
        load_params={"type":"p_boundary_condition0", "f":gravity_*g, "P0":float(pe)},
        res_basename="Fig4-unloaded",
        get_results=1,
        verbose=1)

    phisref_imposed = [numpy.random.uniform(low=0.4, high=0.6) for i in range(len(phisref_computation))]

    ### computing the end-exhalation configuration
    Uexhal, phisexhal, dVunloaded = dmech.run_RivlinCube_PoroHyperelasticity(
        cube_params=cube_params,
```

```
        move_params = {"move":True, "U":Uref},
        porosity_params={"type":"function_xml_from_array", "val":phisref_imposed},
        mat_params=mat_params,
        inertia_params={"applied":True, "rho_val":1e-8},
        step_params={"dt_min":1e-4, "dt_ini":0.125},
        load_params={"type":"p_boundary_condition", "f":gravity_*g, "P0":float(pe)},
        res_basename="Fig4-exhalation",
        get_results=1,
        verbose=1)

    ### computing the end-inhalation configuration
    Uinhal, phisinhal, dVunloaded = dmech.run_RivlinCube_PoroHyperelasticity(
        cube_params=cube_params,
        move_params={"move":True, "U":Uref},
        porosity_params={"type":"function_xml_from_array", "val":phisref_imposed},
        mat_params=mat_params,
        inertia_params={"applied":True, "rho_val":1e-8},
        step_params={"dt_min":1e-4, "dt_ini":0.125},
        load_params={"type":"p_boundary_condition", "f":gravity_*g, "P0":float(pi)},
        res_basename="Fig4-inhalation",
        get_results=1,
        verbose=1)

    if (gravity_ == 0):
        phisexhal_g0 = copy.deepcopy(phisexhal)
        phisinhal_g0 = copy.deepcopy(phisinhal)
```

[ ]:
```
porosity_lst = numpy.linspace(0, 1, 300)

porosity_exhal_g0 = []
porosity_inhal_g0 = []
porosity_exhal_g  = []
porosity_inhal_g  = []
porosity_ref      = []
porosity_plot     = []
for c in range(0, len(porosity_lst)-1):
    min = porosity_lst[c]
    max = porosity_lst[c+1]
    porosity_exhal_g0.append(numpy.sum([min<=i<max for i in phisexhal_g0]))
    porosity_inhal_g0.append(numpy.sum([min<=i<max for i in phisinhal_g0]))
    porosity_exhal_g.append(numpy.sum([min<=i<max for i in phisexhal]))
    porosity_inhal_g.append(numpy.sum([min<=i<max for i in phisinhal]))
    porosity_ref.append(numpy.sum([min<=i<max for i in phisref_imposed]))
    porosity_plot.append(1-(min+(max-min)/2))
```

Generating plots

End-exhalation

[ ]:
```
fig, ax = plt.subplots()

### plotting parameters
plt.rc('xtick', labelsize=18)
plt.rc('ytick', labelsize=18)
plt.rc('axes', labelsize=18)
fig.set_size_inches(8, 6)
plt.xlim([0.3, 0.9])
plt.ylim([0., 14000])
ax.set_ylabel("Frequency", fontsize=22, labelpad=10)
ax.set_xlabel("Porosity", fontsize=22, labelpad=10)
```

```
##### plot results
width = max-min
ax.bar(porosity_plot, porosity_ref    , color="green" , label='$\Phi_{f0}$'  , alpha=0.5,␣
↪edgecolor="black", width=width)
ax.bar(porosity_plot, porosity_exhal_g, color="tomato", label="$\Phi_{fe}$ w/gravity"  ,␣
↪alpha=0.5, edgecolor="black", width=width)
ax.bar(porosity_plot, porosity_exhal_g0, color="blue" , label="$\Phi_{fe}$ wo/gravity",␣
↪alpha=0.4, edgecolor="black", width=width)
ax.legend()

plt.legend(loc="upper left", fontsize=18)
plt.show()
```

End-inhalation

[ ]:
```
fig, ax = plt.subplots()

### plotting parameters
plt.rc('xtick', labelsize=18)
plt.rc('ytick', labelsize=18)
plt.rc('axes', labelsize=18)
fig.set_size_inches(8, 6)
plt.xlim([0.3, 0.9])
plt.ylim([0., 14000])
ax.set_ylabel("Frequency", fontsize=22, labelpad=10)
ax.set_xlabel("Porosity", fontsize=22, labelpad=10)

width = max-min
ax.bar(porosity_plot, porosity_ref     , color="green" , label='$\Phi_{f0}$'  , alpha=0.
↪5, edgecolor="black", width=width)
ax.bar(porosity_plot, porosity_inhal_g , color="tomato", label='$\Phi_{fi}$ w/gravity'  ,␣
↪alpha=0.5, edgecolor="black", width=width)
ax.bar(porosity_plot, porosity_inhal_g0, color="blue"  , label='$\Phi_{fi}$ wo/gravity',␣
↪alpha=0.4, edgecolor="black", width=width)
ax.legend()

plt.legend(loc="upper left", fontsize=18)
plt.show()
```

D Code for Figure 8

Imports

[ ]:
```
import dolfin
import matplotlib.pyplot as plt
import numpy
import pandas

import dolfin_mech as dmech
import get_invariants
```

Parameters

Mesh

[ ]:
```
cube_params = {"path_and_mesh_name":"Data/generic_mesh.xdmf"}
```

Material

[ ]:
```
params = {
    "alpha":0.16,      # kPa
    "gamma":0.5,       # [-]
    "c1":0.8,          # kPa
    "c2":0.2,          # kPa
    "kappa":1e2,       # kPa
    "eta":1e-5,        # kPa
    "rho_solid":1e-6} # g/mm3
mat_params = {"scaling":"linear", "parameters":params}
```

Loading

[ ]:
```
pe = -0.5    # kPa
pi = -3.0    # kPa
g  = +9.81e3 # mm/s2

h_lst = [0., -0.005, +0.005, -0.0065, +0.0065]
```

Computing strain fields

[ ]:
```
invariants = {}

for h in h_lst:

    ### computing the unloaded configuration from a generic end-exhalation configuration
    Uref, phisref_computation, dV_expi_ini = dmech.run_RivlinCube_PoroHyperelasticity(
        inverse=1,
        porosity_params={"type":"mesh_function_random_xml", "val":0.3},
        cube_params=cube_params,
        mat_params=mat_params,
        inertia_params={"applied":True, "rho_val":1e-8},
        step_params={"dt_min":1e-4, "dt_ini":1},
        load_params={"type":"p_boundary_condition0", "f":g, "P0":float(pe), "H":h},
        res_basename="Fig8-unloaded"+str(h),
        get_results=1,
        verbose=1)

    ### computing the end-exhalation configuration
    U_exhal, phisexhal, dV_unloaded = dmech.run_RivlinCube_PoroHyperelasticity(
```

```
        cube_params=cube_params,
        move_params = {"move":True, "U":Uref},
        porosity_params={"type":"mesh_function_random_xml", "val":0.5},
        mat_params=mat_params,
        inertia_params={"applied":True, "rho_val":1e-8},
        step_params={"dt_min":1e-4, "dt_ini":0.125},
        load_params={"type":"p_boundary_condition", "f":g, "P0":float(pe), "H":h},
        res_basename="Fig8-exhalation"+str(h),
        get_results=1,
        verbose=1)

    ### computing the end-inhalation configuration
    U_inhal, phisinhal, dV_unloaded = dmech.run_RivlinCube_PoroHyperelasticity(
        cube_params=cube_params,
        move_params = {"move":True, "U":Uref},
        porosity_params={"type":"mesh_function_random_xml", "val":0.5},
        mat_params=mat_params,
        inertia_params={"applied":True, "rho_val":1e-8},
        step_params={"dt_min":1e-4, "dt_ini":0.125},
        load_params={"type":"p_boundary_condition", "f":g, "P0":float(pi), "H":h},
        res_basename="Fig8-inhalation"+str(h),
        get_results=1,
        verbose=1)

    mesh = dolfin.Mesh()
    mesh_name = str(cube_params["path_and_mesh_name"])
    dolfin.XDMFFile(mesh_name).read(mesh)
    dolfin.ALE.move(mesh, Uref)

    invariants_mesh = get_invariants.get_invariants(U_exhal=U_exhal, U_inhal=U_inhal,␣
↪mesh=mesh)
    invariants["h="+str(h)] = invariants_mesh
```

Generating plots

[Hurtado et al.]'s data

[ ]:
```
J  = pandas.read_table("Data/hurtado_J.dat" , sep="\s+", usecols=["zone", "mean",␣
↪"mean+std", "mean-std"]).to_dict("list")
I1 = pandas.read_table("Data/hurtado_I1.dat", sep="\s+", usecols=["zone", "mean",␣
↪"mean+std", "mean-std"]).to_dict("list")
I2 = pandas.read_table("Data/hurtado_I2.dat", sep="\s+", usecols=["zone", "mean",␣
↪"mean+std", "mean-std"]).to_dict("list")
```

I1

[ ]:
```
fig, ax = plt.subplots()

### plotting parameters
plt.rc("xtick", labelsize=20)
plt.rc("ytick", labelsize=20)
ax.set_xticks(numpy.linspace(1, 10, 10))
plt.xlim([0.9, 10.1])
fig.set_size_inches(6, 6)
plt.grid()

### axis labels
ax.set_xlabel("Zone", fontsize=20, labelpad=10)
ax.set_ylabel("Log Normalized First Invariant", fontsize=20, labelpad=10)
```

```
### error bars
down_up_lst = [[abs(J["mean-std"][i]-J["mean"][i])for i in range(len(J["zone"]))],
 ↪[abs(J["mean+std"][i]-J["mean"][i]) for i in range(len(J["zone"]))]]
mean_lst=[J["mean"][i] for i in range(len(J["zone"]))]
plt.errorbar(invariants["h=0.0"]["zone"], mean_lst, yerr=down_up_lst, capsize=4, fmt="s",
 ↪ecolor = "black", markeredgecolor='black', markerfacecolor='black', label='Hurtado et
 ↪al., 2017')

### curves
plt.plot(invariants["h=0.0"]["zone"]    , invariants["h=0.0"]["I1^"]    , color="green" ,
 ↪linestyle="-", marker="s", label="Model (w gravity), H=0"  )
plt.plot(invariants["h=0.005"]["zone"]  , invariants["h=0.005"]["I1^"]  , color="red"   ,
 ↪linestyle="-", marker="s", label="Model (w gravity), H=+H1")
plt.plot(invariants["h=-0.005"]["zone"] , invariants["h=-0.005"]["I1^"] ,
 ↪color="darkturquoise", linestyle="-", marker="s", label="Model (w gravity), H=-H1")
plt.plot(invariants["h=0.0065"]["zone"] , invariants["h=0.0065"]["I1^"] , color="purple",
 ↪linestyle="-", marker="s", label="Model (w gravity), H=+H2")
plt.plot(invariants["h=-0.0065"]["zone"], invariants["h=-0.0065"]["I1^"], color="orange",
 ↪linestyle="-", marker="s", label="Model (w gravity), H=-H2")
plt.legend(loc="upper right", fontsize=13)
plt.show()
```

I2

[ ]:
```
fig, ax = plt.subplots()

### plotting parameters
plt.rc("xtick", labelsize=20)
plt.rc("ytick", labelsize=20)
plt.xlim([0.9, 10.1])
fig.set_size_inches(6, 6)
ax.set_xticks(numpy.linspace(1, 10, 10))
plt.grid()

### axis labels
ax.set_xlabel("Zone", fontsize=20, labelpad=10)
ax.set_ylabel("Log Normalized Second Invariant", fontsize=20, labelpad=10)

### error bars
down_up_lst = [[abs(J["mean-std"][i]-J["mean"][i])for i in range(len(J["zone"]))],
 ↪[abs(J["mean+std"][i]-J["mean"][i]) for i in range(len(J["zone"]))]]
mean_lst=[J["mean"][i] for i in range(len(J["zone"]))]
plt.errorbar(invariants["h=0.0"]["zone"], mean_lst, yerr=down_up_lst, capsize=4, fmt="s",
 ↪ecolor = "black", markeredgecolor='black', markerfacecolor='black', label='Hurtado et
 ↪al., 2017')

### curves
plt.plot(invariants["h=0.0"]["zone"]    , invariants["h=0.0"]["I2^"]    , color="green" ,
 ↪linestyle="-", marker="s", label="Model (w gravity), H=0"  )
plt.plot(invariants["h=0.005"]["zone"]  , invariants["h=0.005"]["I2^"]  , color="red"   ,
 ↪linestyle="-", marker="s", label="Model (w gravity), H=+H1")
plt.plot(invariants["h=-0.005"]["zone"] , invariants["h=-0.005"]["I2^"] ,
 ↪color="darkturquoise", linestyle="-", marker="s", label="Model (w gravity), H=-H1")
plt.plot(invariants["h=0.0065"]["zone"] , invariants["h=0.0065"]["I2^"] , color="purple",
 ↪linestyle="-", marker="s", label="Model (w gravity), H=+H2")
plt.plot(invariants["h=-0.0065"]["zone"], invariants["h=-0.0065"]["I2^"], color="orange",
 ↪linestyle="-", marker="s", label="Model (w gravity), H=-H2")
plt.legend(loc="upper right", fontsize=13)
```

```
plt.show()
```

J

[ ]:
```
fig, ax = plt.subplots()

### plotting parameters
plt.rc("xtick", labelsize=20)
plt.rc("ytick", labelsize=20)
ax.set_xticks(numpy.linspace(1, 10, 10))
plt.xlim([0.9, 10.1])
fig.set_size_inches(6, 6)
plt.grid()

### axis labels
ax.set_xlabel("Zone", fontsize=20, labelpad=10)
ax.set_ylabel("Log Normalized Third Invariant", fontsize=20, labelpad=10)

### error bars
down_up_lst = [[abs(J["mean-std"][i]-J["mean"][i])for i in range(len(J["zone"]))],␣
 ↪[abs(J["mean+std"][i]-J["mean"][i]) for i in range(len(J["zone"]))]]
mean_lst=[J["mean"][i] for i in range(len(J["zone"]))]
plt.errorbar(invariants["h=0.0"]["zone"], mean_lst, yerr=down_up_lst, capsize=4, fmt="s",␣
 ↪ecolor = "black", markeredgecolor='black', markerfacecolor='black', label='Hurtado et␣
 ↪al., 2017')

### curves
plt.plot(invariants["h=0.0"]["zone"]    , invariants["h=0.0"]["J^"]    , color="green" ,␣
 ↪linestyle="-", marker="s", label="Model (w gravity), H=0"  )
plt.plot(invariants["h=0.005"]["zone"]  , invariants["h=0.005"]["J^"]  , color="red"   ,␣
 ↪linestyle="-", marker="s", label="Model (w gravity), H=+H1")
plt.plot(invariants["h=-0.005"]["zone"] , invariants["h=-0.005"]["J^"] ,␣
 ↪color="darkturquoise", linestyle="-", marker="s", label="Model (w gravity), H=-H1")
plt.plot(invariants["h=0.0065"]["zone"] , invariants["h=0.0065"]["J^"] , color="purple",␣
 ↪linestyle="-", marker="s", label="Model (w gravity), H=+H2")
plt.plot(invariants["h=-0.0065"]["zone"], invariants["h=-0.0065"]["J^"], color="orange",␣
 ↪linestyle="-", marker="s", label="Model (w gravity), H=-H2")
plt.legend(loc="upper right", fontsize=13)
plt.show()
```

E Code for Figure 9

Imports

[ ]:
```
import dolfin
import matplotlib.pyplot as plt
import meshio
import numpy

import dolfin_mech as dmech

import get_invariants
```

Parameters

Mesh

[ ]:
```
cube_params = {"path_and_mesh_name":"Data/generic_mesh.xdmf"}
```

Material

[ ]:
```
params = {
    "alpha":0.16,      # kPa
    "gamma":0.5,       # [-]
    "c1":0.4,          # kPa
    "c2":0.2,           # kPa
    "kappa":1e2,       # kPa
    "eta":1e-5,        # kPa
    "rho_solid":1e-6} # g/mm3
mat_params = {"scaling":"linear", "parameters":params}
```

Loading

[ ]:
```
pe = -0.5    # kPa
pi = -2.0    # kPa
g  = +9.81e3 # mm/s2
```

Computing strain fields in prone and supine positions

[ ]:
```
invariants = {}

gravity_lst = [-1.,+1.]
for gravity_cste in gravity_lst:

    ### computing the unloaded configuration from a generic end-exhalation configuration
    Uref, phisref_computation, dV_expi_ini = dmech.run_RivlinCube_PoroHyperelasticity(
        inverse=1,
        cube_params=cube_params,
        mat_params=mat_params,
        inertia_params={"applied":True, "rho_val":1e-8},
        step_params={"dt_min":1e-4, "dt_ini":1},
        load_params={"type":"p_boundary_condition0", "f":gravity_cste*g, "P0":float(pe)},
        res_basename="Fig9-unloaded",
        get_results=1,
        verbose=1)

    phisref_imposed = [numpy.random.uniform(low=0.4, high=0.6) for i in
↪range(len(phisref_computation))]
```

```
    ### computing the end-exhalation configuration
    U_exhal, phisexhal, dV_unloaded = dmech.run_RivlinCube_PoroHyperelasticity(
        cube_params=cube_params,
        move_params = {"move":True, "U":Uref},
        porosity_params={"type":"function_xml_from_array", "val":phisref_imposed},
        mat_params=mat_params,
        inertia_params={"applied":True, "rho_val":1e-8},
        step_params={"dt_min":1e-4, "dt_ini":0.125},
        load_params={"type":"p_boundary_condition", "f":gravity_cste*g, "P0":float(pe)},
        res_basename="Fig9-exhalation",
        get_results=1,
        verbose=1)

    ### computing the end-inhalation configuration
    U_inhal, phisinhal, dV_unloaded = dmech.run_RivlinCube_PoroHyperelasticity(
        cube_params=cube_params,
        move_params = {"move":True, "U":Uref},
        porosity_params={"type":"function_xml_from_array", "val":phisref_imposed},
        mat_params=mat_params,
        inertia_params={"applied":True, "rho_val":1e-8},
        step_params={"dt_min":1e-4, "dt_ini":0.125},
        load_params={"type":"p_boundary_condition", "f":gravity_cste*g, "P0":float(pi)},
        res_basename="Fig9-inhalation",
        get_results=1,
        verbose=1)

    mesh = dolfin.Mesh()
    mesh_name = str(cube_params["path_and_mesh_name"])
    dolfin.XDMFFile(mesh_name).read(mesh)
    dolfin.ALE.move(mesh, Uref)

    invariants_mesh = get_invariants.get_invariants(U_exhal=U_exhal, U_inhal=U_inhal,␣
↪mesh=mesh, lognorm=False)
    invariants["g="+str(gravity_cste)] = invariants_mesh
```

Post-processing

Reading displacement field from [Patte et al.] and computing associated invariants

[ ]:
```
mesh = dolfin.Mesh()
dolfin.XDMFFile("Data/patte_mesh.xdmf").read(mesh)
fe = dolfin.VectorElement(
    family="CG",
    cell=mesh.ufl_cell(),
    degree=1)
U_fs= dolfin.FunctionSpace(
    mesh,
    fe)

U_inhal_patte = dolfin.Function(U_fs, name="U")
U_exhal_patte = dolfin.Function(U_fs, name="U")

mesh_meshio = meshio.read("Data/patte_mesh.xdmf")
u_meshio = mesh_meshio.point_data["U"]
u_meshio = u_meshio.tolist()
u_meshio = [item for sublist in u_meshio for item in sublist]

c = 0
for dof in dolfin.vertex_to_dof_map(U_fs):
```

```
    U_inhal_patte.vector()[dof] = u_meshio[c]
    U_exhal_patte.vector()[dof] = 0.
    c += 1

invariants_mesh_patte = get_invariants.get_invariants(U_exhal=U_exhal_patte,␣
↪U_inhal=U_inhal_patte, mesh=mesh, lognorm=False)
```

Generating plots

I1

[ ]:
```
fig, ax = plt.subplots()

### plotting parameters
plt.rc('xtick', labelsize=16)
plt.rc('ytick', labelsize=16)
plt.rc('axes', labelsize=16)
plt.ylim([1, 1.9])
plt.xlim([1, 10])
fig.set_size_inches(6, 6)
plt.grid()

### curves
plt.plot(invariants_mesh_patte["zone"], invariants_mesh_patte["I1"], color="green",␣
↪linestyle="-", marker="s", label="Patte et al., 2022")
plt.plot(invariants["g=1.0"]["zone"]  , invariants["g=1.0"]["I1"]  , color="blue" ,␣
↪linestyle="-", marker="s", label="Supine position")
plt.plot(invariants["g=-1.0"]["zone"] , invariants["g=-1.0"]["I1"] , color="red"  ,␣
↪linestyle="-", marker="s", label="Prone position" )
plt.legend(loc="upper right", fontsize=16)

### axis name
ax.set_ylabel("Average of the first invariant per zone")
ax.set_xlabel("Zone")
ax.set_xticks(numpy.linspace(1, 10, 10))

plt.show()
```

I2

[ ]:
```
fig, ax = plt.subplots()

### plotting parameters
plt.rc('xtick', labelsize=16)
plt.rc('ytick', labelsize=16)
plt.rc('axes', labelsize=16)
plt.ylim([1, 3.5])
plt.xlim([1, 10])
fig.set_size_inches(6, 6)
plt.grid()

### curves
plt.plot(invariants_mesh_patte["zone"], invariants_mesh_patte["I2"], color="green",␣
↪linestyle="-", marker="s", label="Patte et al., 2022")
plt.plot(invariants["g=1.0"]["zone"]  , invariants["g=1.0"]["I2"]  , color="blue" ,␣
↪linestyle="-", marker="s", label="Supine position")
plt.plot(invariants["g=-1.0"]["zone"] , invariants["g=-1.0"]["I2"] , color="red"  ,␣
↪linestyle="-", marker="s", label="Prone position" )
plt.legend(loc="upper right", fontsize=16)
```

```
### axis name
ax.set_ylabel("Average of the first invariant per zone")
ax.set_xlabel("Zone")
ax.set_xticks(numpy.linspace(1, 10, 10))

plt.show()
```

J

[ ]:
```
fig, ax = plt.subplots()

### plotting parameters
plt.rc('xtick', labelsize=16)
plt.rc('ytick', labelsize=16)
plt.rc('axes', labelsize=16)
plt.ylim([1, 2.5])
plt.xlim([1, 10])
fig.set_size_inches(6, 6)
plt.grid()

### curves
plt.plot(invariants_mesh_patte["zone"], invariants_mesh_patte["J"], color="green",␣
 ↪linestyle="-", marker="s", label="Patte et al., 2022")
plt.plot(invariants["g=1.0"]["zone"]  , invariants["g=1.0"]["J"]  , color="blue" ,␣
 ↪linestyle="-", marker="s", label="Supine position")
plt.plot(invariants["g=-1.0"]["zone"] , invariants["g=-1.0"]["J"] , color="red"  ,␣
 ↪linestyle="-", marker="s", label="Prone position" )
plt.legend(loc="upper right", fontsize=16)

### axis name
ax.set_ylabel("Average of the first invariant per zone")
ax.set_xlabel("Zone")
ax.set_xticks(numpy.linspace(1, 10, 10))

plt.show()
```